International Journal of Concrete Structures and Materials

RESEARCH

Open Access

Concentric Compressive Performance of Precast Concrete Filled Steel Tube with Intermediate Construction Connection Made of High-Performance Concretes

Ahmed Hamoda[1*], Aref A. Abadel[2], Abedulgader Baktheer[3*] and Mohamed Emara[4,5]

Abstract

Precast concrete-filled steel tubular (CFST) circular columns assembled with connecting joints are commonly employed in building structures. However, there is a lack of research regarding the behavior of precast CFST columns that are connected with construction joints made of high-performance concrete (HPC), such as engineered cementitious composites (ECC) as well as high-strength fiber-reinforced concrete (HSFRC). This paper presents an experimental investigation of precast CFST circular columns subjected to axial loads, tubed with galvanized steel sheets (GSS) and connected with joints made of ECC, HSFRC and normal concrete (NC). Ten slender columns are tested until collapse. The primary studied parameters include the development length along with the connection concrete type. The experimental results reveal that an increase in the development length of the reinforcement, i.e., the length of the connecting concrete joint significantly enhances both the cracking and the load-bearing capacity of slender CFST precast columns that are connected with an intermediate concrete joint. Moreover, the combination of GSS tubes with ECC and HSFRC joints markedly enhances the ultimate load, demonstrating an impressive increase of 115% and 247%, respectively, over the precast NC control column. In addition, three-dimensional nonlinear finite element modeling is performed considering the initially existing imperfection within the precast CFST columns which is validated against the experimentally obtained data. These models are utilized to further investigate parameters, such as GSS thickness and longitudinal reinforcement ratio.

Keywords Precast columns, Concrete-filled steel tubes, Galvanizes steel sheets, Strain hardening cementitious composites, High-strength fiber reinforced concrete, Finite-element modeling

Journal information: ISSN 1976-0485 / eISSN 2234-1315.

*Correspondence:
Ahmed Hamoda
ahmed_hamode@eng.kfs.edu.eg
Abedulgader Baktheer
abedulgader.baktheer@ibnm.uni-hannover.de
[1] Civil Engineering Department, Faculty of Engineering, Kafrelsheikh University, Kafrelsheikh, Egypt
[2] Department of Civil Engineering, College of Engineering, King Saud University, 11421 Riyadh, Saudi Arabia
[3] Institute of Mechanics and Computational Mechanics, Leibniz Universität Hannover, 30167 Hannover, Germany
[4] Structural Engineering Department, Faculty of Engineering, Zagazig University, B.O. Box 44519, Zagazig, Sharkia, Egypt
[5] Department of Civil Engineering, Delta Higher Institute for Engineering & Technology, Talkha, Egypt

1 Introduction

Concrete-filled steel tube (CFST) represents a composite column configuration achieved by filling a steel tube with concrete, a method widely recognized for its performance of load bearing capacity in structures (Ci et al., 2022a; Gopal & Manoharan, 2006; Liao et al., 2013; Xiong et al., 2024). In particular, CFSTs are widely used in high-rise buildings and bridge piers due to their ability to withstand significant axial loads. In this type of structural element, the steel tube not only confines the concrete core but also acts as permanent formwork, which streamlines the construction process (Ci et al., 2022b; Hu et al., 2023; Isleem et al., 2023; Liu et al., 2023). CFST columns offer significantly higher strength, ductility and resistance to fire and seismic forces compared to conventional reinforced concrete columns.

The prefabrication of precast CFST columns in controlled factory settings emerges as an advantageous solution, significantly reducing the activities on the construction site, including the formwork preparation, the reinforcement placement, the concrete casting and curing. These streamlined processes not only expedite construction but also contribute to substantial reductions in carbon emissions associated with each project (Hamoda et al., 2023a). Despite these advantages of precast CFST, challenges arise due to transportation limitations, as precast columns are typically constrained by length restrictions, necessitating the use of multiple connected columns to achieve the desired length. In addition, column splices are often required on-site, driven more by erection conditions than structural necessity. However, connecting multiple precast CFST columns offers structural versatility and adaptability, allowing for efficient customization of lengths, sizes, and configurations to suit diverse project needs. This approach streamlines construction, enhances design flexibility, and promotes innovation in building design, ultimately contributing to resilient and sustainable built environments.

Several studies have been carried out previously on the load-bearing behavior of traditional RC columns (Elwood & Eberhard, 2009; Hamoda et al., 2024a; Ma et al., 2012; Saatcioglu & Ozcebe 1989). These studies have shown that the structural behavior of RC columns depends mainly on its longitudinal and transverse reinforcement ratio. The failure modes of RC columns can vary depending on factors, such as size and applied loads, and include phenomena, such as cover concrete crushing, rebar buckling, bending as well as combined failure modes (Abadel et al., 2022; Obaidat et al., 2020). Recently, research efforts have focused on studying the structural response of precast concrete (PC) columns (Kuttab & Dougill, 1988; Rave-Arango et al., 2018; Tadi Beni & Madhkhan, 2022). For example, Xu et al. (2023) conducted experiments on PC columns to analyze the effects of different classes of concrete, reinforcement configurations and axial compressive loading on fire resistance. Interestingly, their findings indicated better fire behavior for columns of low-strength concrete compared to those made of high-strength concrete.

In recent years, an increasing body of comprehensive studies have been conducted to assess the bearing capacity of CFST columns under both axial as well as lateral loading (Gu et al., 2024; Zhou et al., 2023). For example, Ekmekyapar and AL-Eliwi (2016) studied the behavior of circular CFST columns under axial loading, examining different ratios of column length to diameter (L/D), column diameter to steel tube thickness (D/t), steel grades and concrete classes in their testing program. Their results underline the direct influence of the L/D ratio on column behavior, while the D/t ratio has no significant influence. In addition, Liu et al. (2023) investigated the size effect of circular CFST columns subjected to axial compression and revealed discrepancies between current design codes and experimental results, especially in overestimating the peak capacity of short CFST columns with large diameter. In addition, Ci et al. (2022b) conducted experimental investigations on circular concrete-filled double steel tube columns under axial loading, focusing on the slenderness ratio of the column and the thickness of the internal steel tube. Their results are consistent with those of previous studies and show that the ultimate strength decreases with increasing slenderness of the column and that the inner steel tube thickness shows only a marginal influence on the column strength. Furthermore, the axial compression behavior of columns reinforced with stainless steel tubes and FRP grids has been thoroughly investigated in Huang et al. (2023); Hu et al., 2024).

Investigating the performance of precast concrete columns with connecting joints has been a focus of recent research, although there are still few references that specifically address the characterization of such connections. A recent experimental study by Hamoda et al. (2024b) investigated the axial behavior of slender RC precast columns having circular cross section and a normal concrete intermediate joint. Their comprehensive test program investigated the impact of the ratio of the longitudinal reinforcement as well as the development length of the embedded steel bars on the axial behavior of precast columns and showed significant improvements with increasing reinforcement ratio and embedment length. The seismic response of PC columns containing bolted joints consisting of column shoes, bolts and grout was investigated by Wang et al. (2020). Their experimental results showed that PC columns with hybrid connections exhibit comparable seismic behavior to cast-in-place

concrete columns in the mid-story height range. In addition, Tullini and Minghini (2016) conducted an experimental program focusing on full-scale precast concrete column connections containing grouted joints and subjected to different loading conditions. Their results emphasized the effectiveness of stress transfer along the joint area. In addition, Hu et al. (2017) investigated bolted end-plate connections, which exhibited structural behavior similar to that of cast-in-place concrete columns. These collective efforts shed light on the diverse connection possibilities for precast concrete columns and their effects on load-bearing capacity.

In modern construction practice, the trend is increasingly moving towards replacing normal concrete (NC) with high-performance concrete (HPC) as well as fiber-reinforced concrete (FRC) to enhance the strength and structural performance of concrete under wide range of load configurations and scenarios (Baktheer et al., 2022, 2024a; Li et al., 2023). A subtype of HPC, engineered cementitious composites (ECC) are mainly characterized by their hardening behaviour after cracking (Chiadighikaobi et al., 2024; Hamoda et al., 2024c; Wei et al., 2022; Zhang et al., 2023). Compared to NC, ECC has higher flexural and tensile strengths as well as higher ductility (Dong et al., 2022; Hamoda et al., 2023b; Lai et al., 2023). High-strength fiber-reinforced concrete (HSFRC), which is fortified with steel fibers, also exhibits improved mechanical properties. In addition, both ECC and HSFRC contribute to a reduction in crack widths, which can minimize corrosion and concrete deterioration (Xu et al., 2021). Their use in structural elements has shown promise in improving flexural properties, ductility and failure modes (Dong et al., 2022; Hung et al., 2023; Lai et al., 2023). These advances in concrete technology have been applied in reinforced concrete (RC) and precast columns. For example, Emara et al. (2023) compared the behavior of RC columns from ECC with NC columns exposed to axial loading, showing that ECC columns with fibers content of 1.5% polypropylene had demonstrated better ultimate compressive strength, ductility as well as durability. In addition, Hu et al. (2023) studied the axial compression response of square tubular steel columns filled with HSFRC and found that although the addition of steel fibers did not change the failure modes, the post-peak behavior improved with increasing fiber volume fraction. In addition, Hamoda et al. (2023a) investigated the use of HPC in the intermediate connection of precast concrete (PC) columns using strain-hardening cementitious composites (SHCC) as well as ECC. The results showed that cracking and load-bearing capacity increase significantly with longer steel bars and higher reinforcement ratios. In addition, the increasing use of galvanized steel tubes in concrete-filled tubular steel columns (CFST) in recent years underlines their beneficial properties, including high corrosion resistance, stability and load-bearing capacity (Fang et al., 2020).

The current literature reveals a significant gap in understanding the behavior of precast columns connected with normal and high-performance concrete, especially in the context of concrete-filled steel tubular columns (CFST) with high performance composite connections, such as ECC or HSFRC. To address this gap, this study aims to evaluate the effectiveness of this innovative approach in comparison with typical PC columns with NC connections. Through tests on circular slender PC columns under axial compression with different embedded lengths, to capture their behavior until collapse. Using 3D nonlinear finite element models (FEM), that validate the experimental results, the impact of longitudinal reinforcement ration as well as the thickness of the galvanized steel sheet (GSS) on the performance of precast CFST columns connected with high performance concrete is investigated.

2 Experimental Program

2.1 Description of the Specimens and Investigated Parameters

Ten slender PC columns with circular cross section were fabricated and subjected to monotonic compressive axial load until failure. To evaluate the improvement in capacity of the slender PC columns using precast NC filled in circular GSS tubes for the upper and lower part of the column as shown in Fig. 1 and using different intermediate concrete connection types, a normal slender RC column without intermediate connection and without circular GSS tubes with total length of 750 mm was additionally tested and regarded as a control specimen.

This study focuses on the performance of slender CFST circular columns, characterized by slenderness ratios (λ) up to 29, tested under axial loading until collapse. The research deliberately investigates slender CFST circular columns to explore their vulnerability to buckling, phenomena intrinsic to members with high slenderness ratios. The primary objective is to evaluate the criticality of intermediate construction joints on such columns and their impact on the load-carrying capacity and stability. Specifically, the study examines the influence of the embedded development length (L_d) of (4D, 16D, and 18D) and the concrete type used in the joint connection. By maintaining a slenderness ratio within a controlled range and ensuring that it remains below the critical buckling threshold, the study isolates the effect of the joint and development length parameters, minimizing potential confounding factors. This focused approach aims to provide a quantitative assessment of joint efficiency and

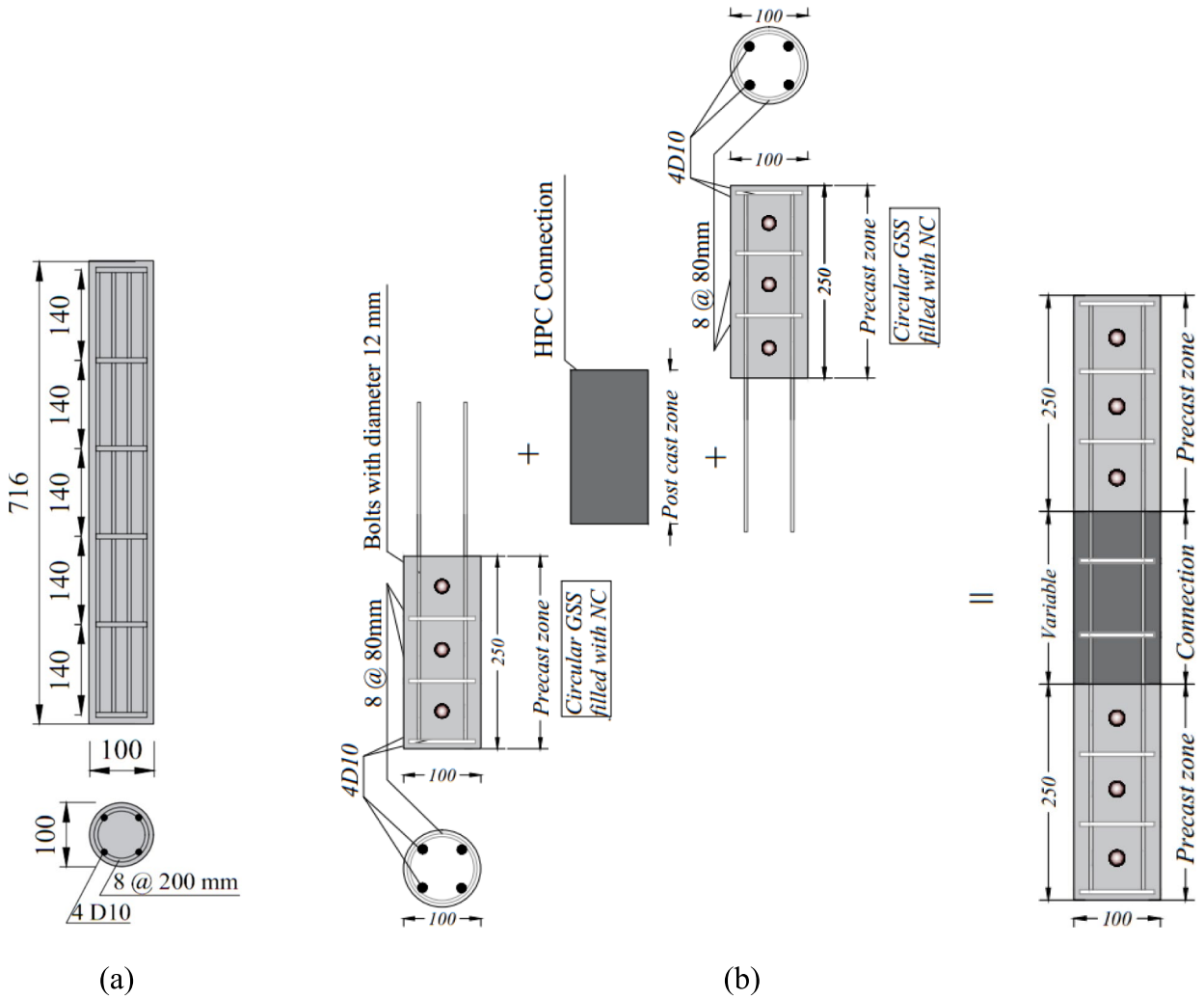

Fig. 1 Reinforcement geometric details for the proposed columns. **a** Master C0 column. **b** CFST column (Units: in mm)

Table 1 Details of the tested columns

Group	Column`s ID	Identical details	Variable details	
			Type of HPC connection	Development length (L_d)
Control	C0	NC circular column	–	–
G-N	N-L1	= Precast NC filled inside circular tube of GSS with 0.5 mm thick = Circular NC columns with 100 mm diameter and 250 mm length = Reinforcement: 4D10 encircled with 8 mm stirrups each 80 mm = Width-to-depth ratio is 200	NC	14D
	N-L2			18D
	N-L3			22D
G-E	E-L1		ECC	14D
	E-L2			18D
	E-L3			22D
G-H	H-L1		HSFRC	14D
	H-L2			18D
	H-L3			22D

its implications for the stability and strength of slender structural members.

Within the test program, two parameters were investigated, namely, the type of concrete connection (NC, ECC and HSFRC) as well as L_d of the embedded steel bars or connecting concrete joint, whereby three different embedment lengths of 14D, 18D and 22D were investigated as summarized in Table 1, where D represents the bar diameter. The tested columns with intermediate connection were categorized into three groups depending on the type of connection. For the naming of the tested columns, "N" stands for NC, "E" for ECC and "H" for HSFRC and the second number L1, L2 and L3 stands for the development length of the embedded steel bars of 14D, 18D and 22D, respectively.

The columns comprised three segments, two of which consisted of precast NC-filled circular GSS tubes joined together by an intermediate joint of NC, ECC or HSFRC, as shown in Fig. 1. All columns were circular and had a diameter of 100 mm. The upper and lower part of the precast NC had a length of 250 mm, while the intermediate part had a different length depending on the investigated length of the embedded steel bars (see Fig. 1). All columns had the same reinforcement with 4D12 as longitudinal reinforcement and ring stirrups in a closed form with an 8 mm diameter, which were arranged at a vertical distance of 80 mm.

2.2 Material Properties and Mix Proportion

The specimens were produced using a ready mix of NC, ECC, and HSFRC, with their respective mix proportions outlined in Table 2. From Table 2, it is apparent that ECC requires a larger amount of cement as well as high-range water reducer in comparison with SHFRC. Thus, for economic considerations, SHFRC emerges as the more favorable choice for filling the joint connection of precast columns.

To characterize the properties of the materials used within the test program, both uniaxial tension as well as uniaxial compression tests were performed. The compression tests were performed using 150 mm × 300 mm cylinders on the same experimenting day. Tests in uniaxial tension were performed using dog bone specimens in compliance with the recommendations of the ACI (2019), as shown in Fig. 2e. The compressive and tensile strengths of all concrete types, including NC, ECC and HSFRC, as well as the recorded strains at f_c' and f_t and the maximum strains are outlined in Table 3. The direct tensile stress–strain performance for ECC and HSFRC with the tests shown in Fig. 2b was idealized.

In addition, tensile tests were performed on coupons to evaluate the mechanical characteristics of the galvanized steel sheets and the steel bars used (see Fig. 2c, d). The recorded tensile stress–strain response of steel bars, steel bolts and galvanized steel sheets are shown in Fig. 2b together with idealized multilinear uniaxial tension laws. The yield stress of the 8 mm steel bars was determined to be 289 MPa, while that of the 12 mm bars was measured at 345 MPa. In terms of tensile strength, the 8 mm bars exhibited a strength of 441 MPa, whereas the 10 mm bars had a tensile strength of 552 MPa. For the galvanized steel sheet, the yield stress was recorded as 235 MPa, with a corresponding tensile strength of 357 MPa.

2.3 Preparation and Production of CFST Precast Columns

As illustrated in Fig. 3a**,** circular steel tubes were fabricated using galvanized steel sheets fastened with three steel bolts. These tubes were then filled with NC to produce two precast CFST panels for each column to be tested. The precast CFST panels had a height of 250 mm and additional lengths for the connections (L_d) of 14D, 18D and 22D which were previously reported (Fayed et al., 2023; Hossain et al., 2015).

To construct the full-length columns, two precast CFST panels, each 250 mm long, were assembled together in opposite directions, leaving a gap (L_d) for casting NC, ECC or HSFRC inside, as depicted in Fig. 2b, c. As an example, the combination of two precast CFST panels having a length of 250 mm joined with $L_d = 168$, 216 and 264 resulted in a total column length of 668 mm, 716 mm and 764 mm, giving slenderness ratios within ranges of 27–29, respectively, according to ECP-203 (2018). The chosen different embedded lengths, giving smaller variation in total slenderness, were selected to minimize the reflection of the slenderness ratio and to examine the influence of the embedded length parameter.

Table 2 Mix proportion

Concrete	Cement with 52.5R (kg/m^3)	F.Agg (kg/m^3)	C.Agg. (kg/m^3)	F.A. (kg/m^3)	W/b	PP (%)	HRWR (kg/m^3)
NC	355	698	1143	–	0.42	–	–
ECC	558	436	–	665	0.23	2.20	15
HSFRC	471	672	1090	28	0.30	2.00	9.6

Cement grade 52.50 N/mm^2, *F.Agg.* fine aggregate, *C.Agg.* coarse aggregate, *F.A.* fly ash, *W/b* water-to-bender ratio (bender = Cement + F.A), *PP* polypropylene fiber, *HRWR* high range water reducer

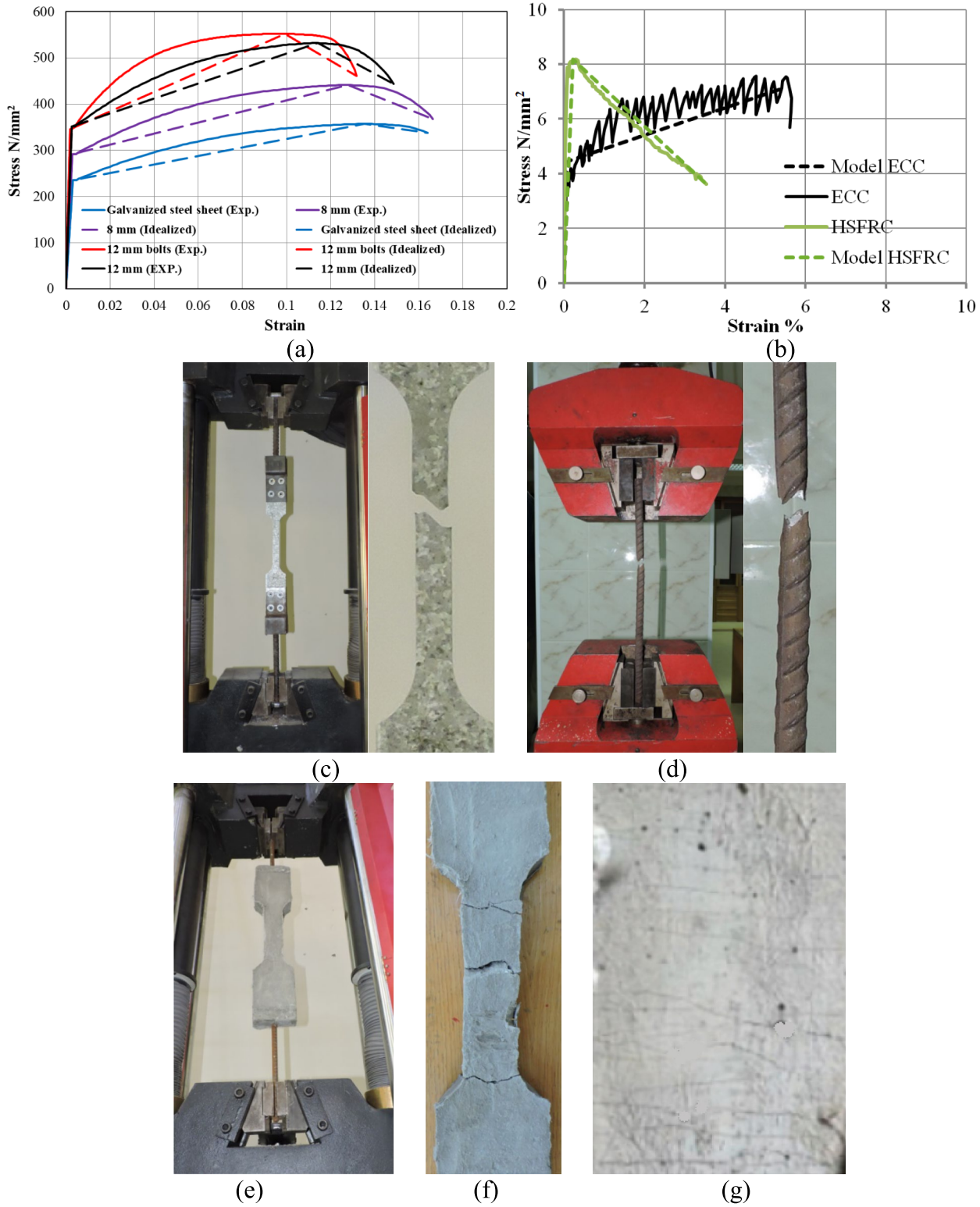

Fig. 2 Uniaxial tensile tests: **a** steel tensile stress–strain curves, **b** concrete tensile stress–strain curves, **c** GSS experimental test, **d** steel bar experimental test, **e** concrete sample direct tensile test, **f** failed HSFRC sample, and **g** cracks of the experimented ECC samples

Table 3 Concrete properties

Concrete type	Compression			Tension		
	$f_{c'}$ (N/mm^2)	Strain at $f_{c'}$	Maximum strain	Maximum elastic f_t (N/mm^2)	Strain at f_t	Maximum strain
NC	32	0.002	0.003	2.76	0.0002	0.0015
ECC	47	0.0031	0.005	3.98	0.0018	0.059
HSFRC	75	0.00017	0.0038	8.1	0.0023	0.036

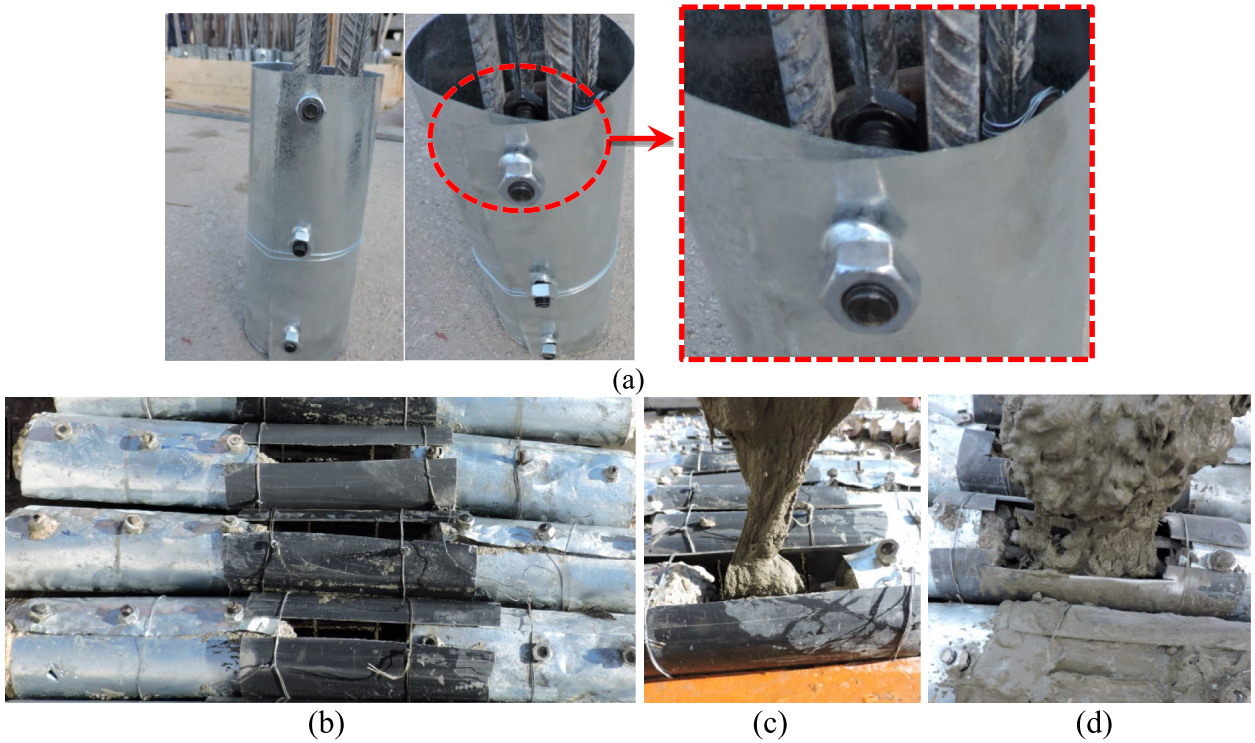

Fig. 3 Construction and assembling of the CFST columns: **a** reinforcement and embedded bolted connectors, **b** arrangement of columns for filling of the intermediate construction joint, **c** flowable PE-ECC, and **d** casting of HSFRC

The connection between the precast CFST columns and the NC/ECC/HSFRC infill was facilitated by a cylindrical formwork, as illustrated in Fig. 3b, c, d, into which castable NC/ECC/HSFRC material could be poured.

To guarantee the quality of the intermediate construction connections, multiple measures were taken during the preparation and assembly of the precast CFST columns. These included ensuring precise alignment of the cross section and minimizing eccentricity, carefully concreting the connection zone to achieve proper bonding, and positioning the embedded reinforcement accurately within the joint. In addition, efforts were made to ensure that the concrete surface of the precast CFST columns matched the properties of the connection material, ensuring uniformity across the joint.

2.4 Experimental Setup and Measuring Techniques

The test program presented in this study was conducted in the testing laboratory of Kafrelsheikh University in Egypt. Using a 1000 kN hydraulic jack securely fixed to a stiff steel frame, the circular precast slender CFST columns were subjected to an axial compressive force as illustrated in Fig. 4. The base of the column was fixed in all directions to prevent any movement or rotation. On the other hand, the upper part of the column was only free to allow the movement in the axial direction in which the load was applied. The same boundary conditions were applied to all columns.

Linear variable displacement transducers (LVDTs) were strategically positioned vertically to measure the vertical displacement resulting from the axial load, as depicted

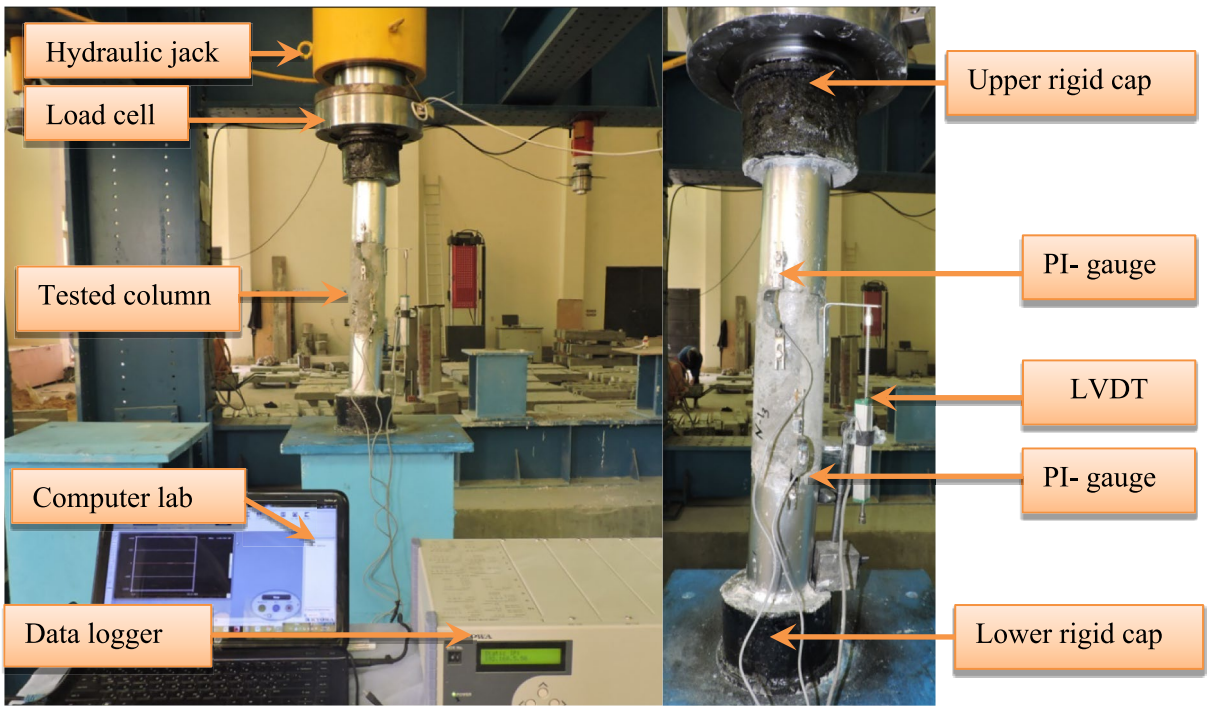

Fig. 4 Test setup and instrumentation

in Fig. 4. In addition, two PI displacement transducers were utilized to measure the crack opening displacement occurring on the surface of the concrete column (see Fig. 4). Subsequently, all of these transducers were connected to a system for collecting recorded data to facilitate automatic recording during the experimentation process, as illustrated in Fig. 4.

3 Experimental Results and Related Discussion

3.1 Deformed Shape and Failure Mode

The evaluated values of crack loading ($\mathbf{P_{cr}}$) as well as the ultimate loading ($\mathbf{P_u}$) are summarized in Table 3 together with the corresponding vertical displacements ($\mathbf{\Delta_{pcr}}$ and $\mathbf{\Delta_{pu}}$) and the failure mode. Figure 5a shows the failure pattern exhibited in the control specimen C0, while Fig. 5b–j illustrates the failure modes observed in the precast CFST columns with NC, ECC and HSFRC connections, respectively.

The control column, C0, exhibited a concrete crushing failure, as depicted in Fig. 5a. In contrast, all precast CFST columns exhibited a combined failure mode, characterized by concrete crushing at the intermediate NC/ECC/HSFRC connection. This was often accompanied by rippling of the GSS of the tubed column, with occasional instances of column buckling.

Columns with an embedded length of 18D, as well as those featuring HSFRC intermediate joints, exhibited buckling, as illustrated in Fig. 5. Notably, columns with ECC intermediate joints displayed hairline cracks in the concrete connection, as exemplified in Fig. 5g. A distinct pattern emerged in the location of concrete crushing within the columns: for those with NC joints, the crushing extended along the entire length of the concrete joint (Fig. 5b, c), whereas in columns with ECC and HSFRC joints, it primarily occurred at the interface between the precast CFST and the intermediate joints (Fig. 5f, g, h).

Furthermore, a closer examination revealed nuanced differences in failure behavior. In columns with HSFRC joints and an embedded length of 18D, only localized interface failure was observed, without clear cracking of the concrete connection (Fig. 5i). Moreover, in columns with HSFRC joints and embedded lengths of 22D, failure was more pronounced in the precast CFST parts of the beam, as depicted in Fig. 5j. This observation underscores the influence of both joint type and embedded length on the distribution of failure mechanisms within the CFST columns.

The crack width ($\mathbf{w_{cr}}$) at the connection interface of the columns corresponding to the cracking load $\mathbf{P_{cr}}$, measured through the PI gauges (Fig. 4), exhibited a decrease in value as the embedded length increased, as outlined in Table 4. Notably, columns with NC joints displayed the highest crack width values, whereas those with HSFRC joints demonstrated the smallest crack width values.

(a)

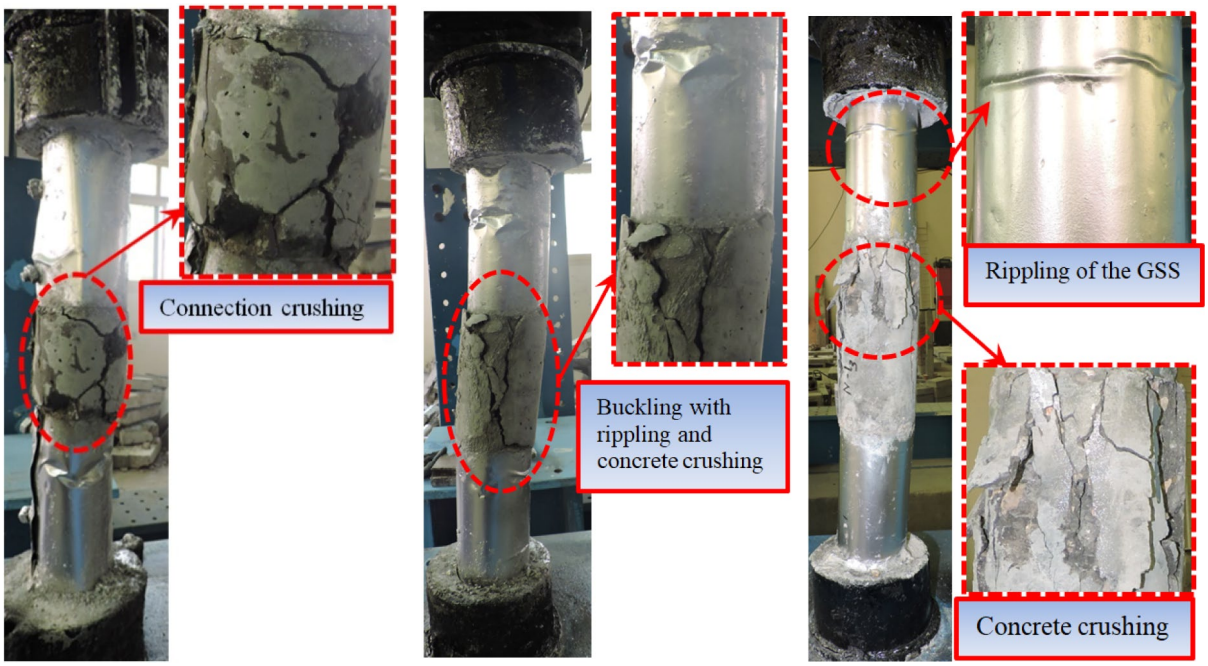

(b) (c) (d)

Fig. 5 Failure mode of the tested columns: **a** Column C0, **b** Column N-L1, **c** Column N-L2, **d** Column N-L3, **e** Column E-L1, **f** Column E-L2, **g** Column E-L3, **h** Column H-L1, **i** Column H-L2, and **j** Column H-L3

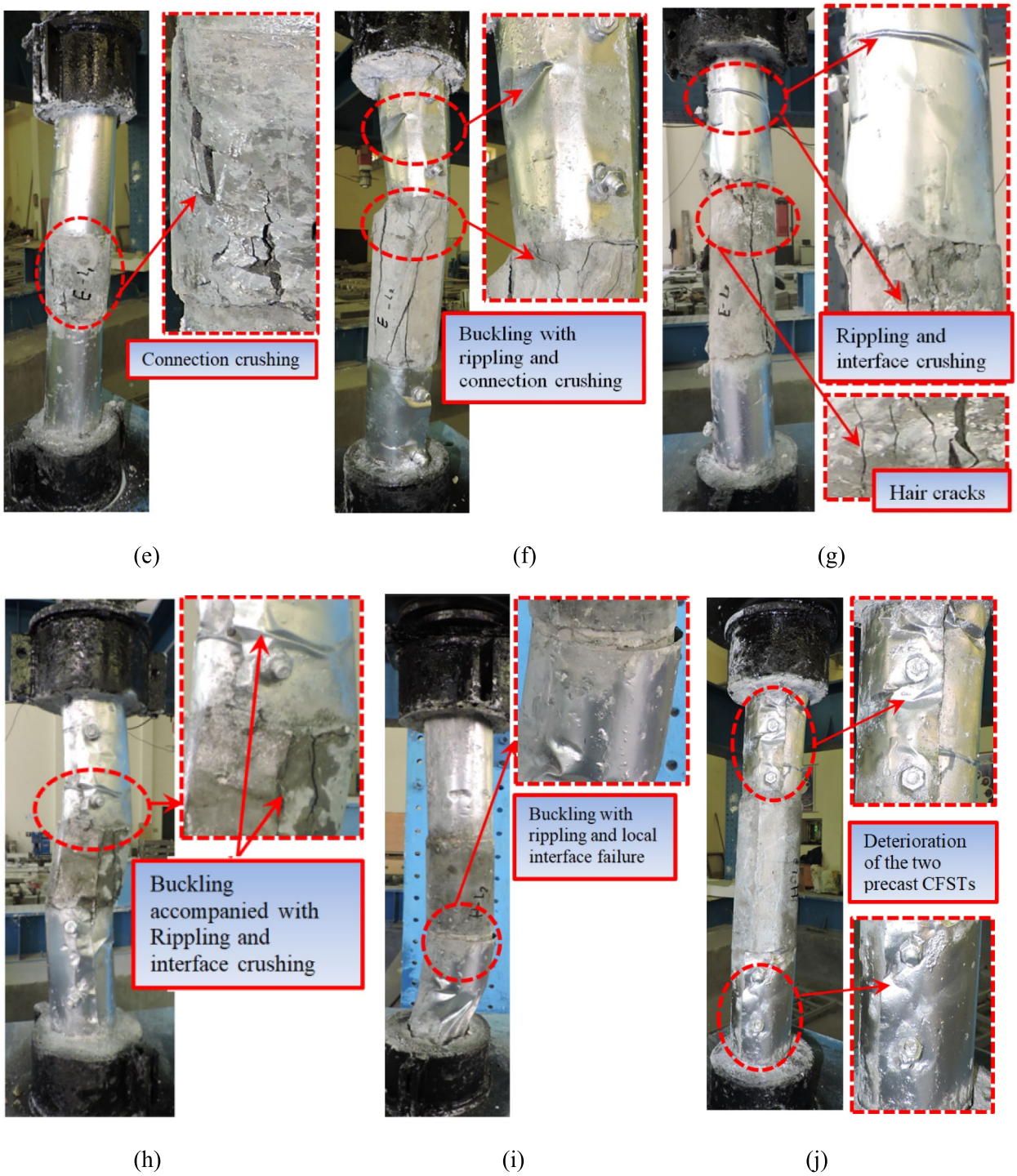

Fig. 5 continued

3.2 Cracking and Ultimate Loads

Table 4 provides a summary of the recorded loads at which the first crack appears ($\mathbf{P_{cr}}$) and the ultimate loads ($\mathbf{P_u}$) for all columns. The ECP-203 (2018) provided close prediction to the NC circular column giving small underestimation of 4%, as shown in Table 4. The close agreement between the experimental and theoretical values indicates that the ECP-203 code (ECP, 2018) provides a reliable estimate of the circular column's capacity. However, the slight difference also highlights the importance of experimental validation to

Table 4 Test obtains

Group	Column's name	Crack stage				Ultimate stage			linear stiffness		Absorbed energy		*Feature and mode of failure
		P_{cr} (kN)	P_{cr}/P_{crC0}	Δ_{Pcr} (mm)	w_{cr} (mm)	P_u (kN)	P_u/P_{uC0}	Δ_{Pu} (mm)	K	K/K_{C0}	J	J/J_{C0}	
Control	C0 EXP	98.00	1.00	6.54	0.20	115.52	1.00	7.50	14.98	1.00	899.12	1.00	C
	C0-ECP (ECP, 2018)					112	0.96						
	C0-Nominal (ECP, 2018)					172	1.50						
GN	N-L1	89.00	0.91	6.44	0.28	107.64	0.93	7.74	13.82	0.92	827.20	0.92	C at Cn. + R
	N-L2	112.00	1.14	7.00	0.26	126.00	1.09	7.70	16.00	1.07	982.80	1.09	B with C at Cn. + R
	N-L3	132.00	1.35	6.84	0.24	149.36	1.29	8.08	19.29	1.29	1299.95	1.45	C at Cn. + R
GE	E-L1	162.00	1.65	7.32	0.20	171.32	1.48	8.90	22.13	1.48	1552.42	1.73	C at Cn. with HC + R
	E-L2	182.00	1.86	7.06	0.20	197.25	1.71	8.62	25.78	1.72	1690.85	1.88	B with C at Cn. with HC + R
	E-L3	235.00	2.40	6.71	0.18	248.08	2.15	8.05	35.00	2.34	2306.63	2.57	C at Cn. with HC + R
GH	H-L1	240.00	2.45	8.28	0.18	258.47	2.24	9.42	29.00	1.94	2524.05	2.81	C at Cn. + R
	H-L2	–	–	–	0.14	375.59	3.25	10.49	–	–	4228.34	4.70	B with C at Cn. + R
	H-L3	–	–	–	0.14	400.80	3.47	10.72	–	–	4625.78	5.14	B with C at Cn. + R

P $_{cr}$ force recorded at the visual hair crack, ***Δ*** $_{Pcr}$ vertical displacement recorded at P_{cr}, ***P*** $_{u}$ ultimate load, ***Δ*** $_{Pu}$ vertical displacement recorded at P_u, ***K*** elastic stiffness index, ***J*** absorbed energy

* Mode of failure: ***C*** concrete crushing, ***Cn***. connection, ***R*** rippling of GSS of the tubed column, ***B*** buckling, ***HC*** hair cracks

account for actual condition. It can be mentioned that the ECP-203 (2018) recommends the ultimate strength equation, used for estimated nominal strength ($\mathbf{P_n}$) as well, in a form presented in Eq. 1 as follows:

$$P_u = \frac{0.67 * \varphi_c * f_c' * A_c}{\gamma_c} + \frac{A_s * \varphi_s * f_y}{\gamma_s} \quad (1)$$

$$P_n = \frac{0.67 * \varphi_c * f_c' * A_c}{1} + \frac{A_s * \varphi_s * f_y}{1} \quad (2)$$

where

f_c` is the concrete compressive strength, γ_c is a factor of safety can be taken as 1.75, A_c is the concrete area cross section, A_s area of the reinforcement, γ_s is a factor of safety can be taken as 1.34, f_y is the steel yield strength, ϕ_c and ϕ_s are the reduction factor for circular section according to the boundary conditions can be considered as 0.65 and 0.62, respectively.

Notably, the cracking force recorded in all precast CFST columns with intermediate joints exceeded that of the control specimen, except for the shortest column with NC connection (i.e., with an embedded length of 14 D), which amounted to approximately 0.91 of the cracking load of the control column. For instance, columns NC-L2 and NC-L3 exhibited cracking loads that were 14% and 35% larger than the control NC column, respectively. In the case of columns with ECC joints, the cracking loads for ECC-L1, ECC-L2, and ECC-L3 were 65%, 86%, and 140% of the cracking load of the control column C0, respectively. Similarly, for columns with HSFRC joints, only column HSFRC-L1 experienced a cracking load that was 145% higher than the control column C0.

It is evident that the delay in the first crack occurrence in all tested precast CFST columns correlates with the increase in the development length of the longitudinal bars, consequently elevating the characteristic cracking force ($\mathbf{P_{cr}}$). Table 4 demonstrates this trend clearly. For instance, increasing the development length from 14 to 18D, and then to 22D in the precast columns with NC joints resulted in an increment in the cracking load by 26% and 48% accordingly. In similar way, for the columns with ECC joints, the cracking force saw increments of 12% and 45%, respectively, when the embedded length was increased from 14 to 18D and 22D. The observed trend aligns with the experimental results documented in Hamoda et al., 2023a for circular PC columns with connecting joints made of HPC. Among the three investigated types of intermediate joints, columns with HSFRC joints exhibited the largest cracking load compared to NC and ECC joints.

The recorded ultimate load in all precast CFST columns tested with intermediate joints, comparable in length to the NC control specimen C0 (i.e., columns that have a development length of 22D and total length of 764 mm), exceeded that of C0. Utilizing GSS tubes enhanced the ultimate load of column NC-L3 by 29% compared to the control column C0. Moreover, combining GSS tubes with ECC and HSFRC joints resulted in remarkable increases in the ultimate load, with increments of 115% and 247%, respectively.

The trend of increasing embedded length leading to higher ultimate loads is evident from Table 4. For example, in columns with ECC joints, increasing the embedded length from 14 to 18D and then to 22D resulted in incremental ultimate load increases of 15% and 45%, respectively. This trend was similarly observed for columns with NC and HSFRC joints. Consistently, among the three types of investigated intermediate joints, columns with HSFRC joints demonstrated the largest ultimate load compared to those with NC and ECC joints.

3.3 Load–Deflection Response

The load–vertical displacement development of all experimented columns are shown in Fig. 6, with the vertical displacements measured at the cracking force and at the ultimate force listed in Table 4. In general, all columns exhibited a linear response up to crack development, whereby the elastic load limits increased with increasing intermediate joint length. From Fig. 6a and Table 4, it is evident that the recorded displacements at which the first crack occurs and the failure loads for the columns with NC joints are relatively close to those of the NC control column. In contrast, larger values were recorded for columns with ECC joints, while the columns with HSFRC joints exhibited the largest vertical displacements at the ultimate load. An increasing vertical displacement at ultimate load was observed for columns with HSFRC joints with the increase of the embedded length, whereas a decreasing trend was observed for columns with ECC joints. Figure 6 illustrates that all columns enter the plastic phase with hardening behavior until reaching the ultimate load. It is worth noting, however, that columns with ECC connections showed softer behavior after the ultimate load until final failure, as shown in Fig. 6b.

3.4 Absorbed Energy and Elastic Stiffness

The energy absorbed (J) of all columns was computed from the overall area below the load–displacement curve, using the approach commonly used in literature [e.g., (Abadel et al., 2024; Gopal & Manoharan, 2006; Punurai et al., 2013)]. Table 4 contains a comparison of the calculated energy J values for all tested columns. The utilization of the GSS tube resulted in improved energy absorption. For instance, comparing column NC-L3 with

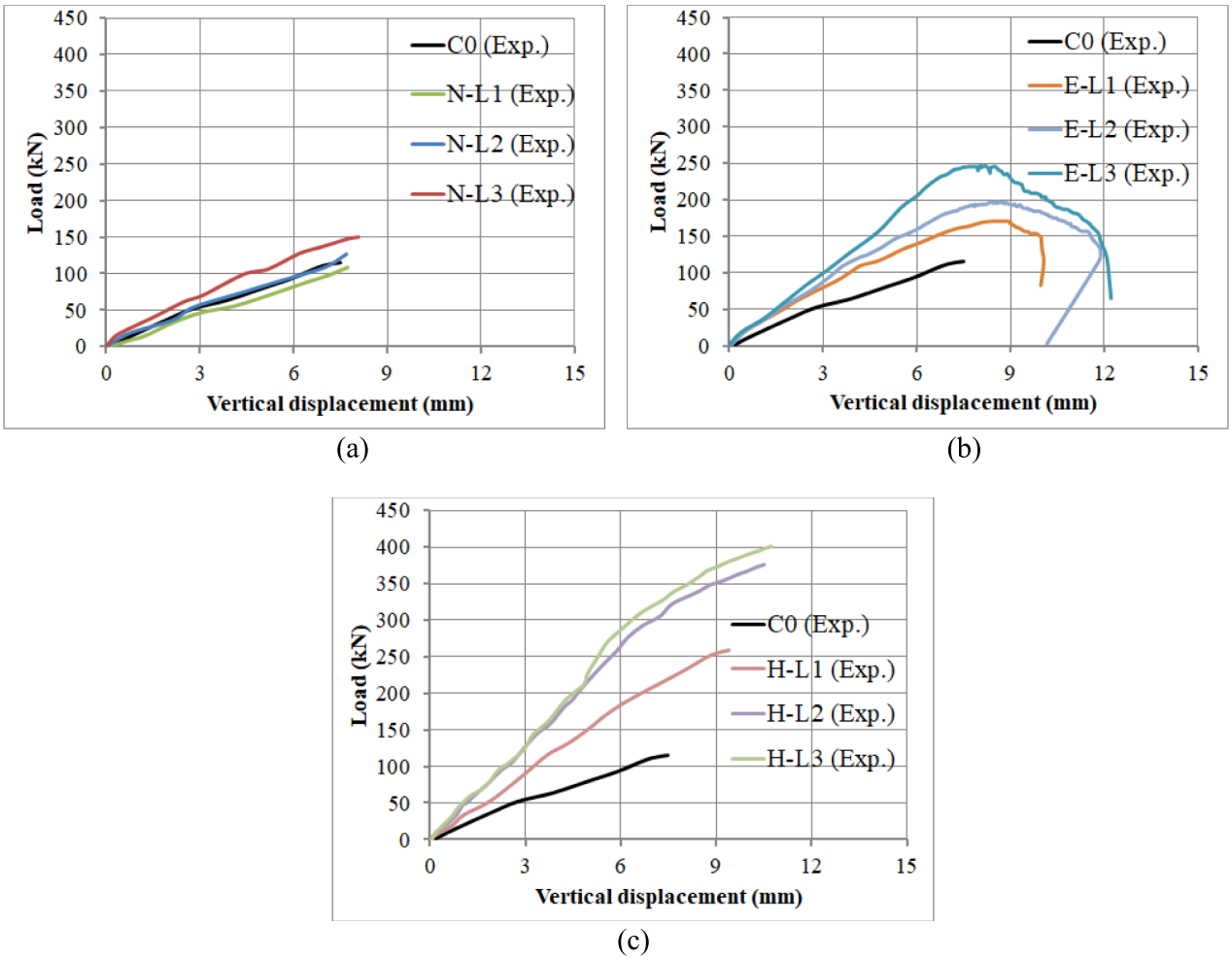

Fig. 6 Load–vertical displacement development: **a** Group GN, **b** Group GE, and **c** Group GH

a total length of 764 mm to the control column with a total length of 750 mm, Table 4 indicates a 45% increase in energy absorption. This enhancement can be attributed to the confinement effect introduced by the GSS steel tube. Furthermore, incorporating ECC with strain hardening behavior and HSFRC with crack bridging effect in the intermediate joint, along with the GSS tubes, resulted in a significant and remarkable improvement in energy absorption compared to the NC column. For instance, when comparing column ECC-L3 and HSFRC-L3, both with a total length of 764 mm, to the control column with a total length of 750 mm, Table 4 demonstrates energy absorption increases of 157% and 414%, respectively.

The elastic stiffness values (K) recorded in all columns are listed in Table 4 which are defined in terms of the linear response slope of the relationship between load and vertical deformation. With the exception of column N-L1, all precast CFST slender columns with NC/ECC/HSFRC connections exhibited larger elastic stiffness in comparison with the control specimen C0. For instance, the NC-L2 and NC-L3 columns exhibited 7% and 29% higher elastic stiffness, respectively, than the NC control column C0. In similar way, columns ECC-L1, ECC-L2, and ECC-L3 exhibited elastic stiffness values 48%, 72%, and 134% larger than the C0 column, respectively. Comparing the stiffness values (K) of the three types of joints for the shortest column with a total length of 668 mm, the HSFRC joint resulted in the largest stiffness among the three types of joints, as summarized in Table 4. Considering columns with a total length of 764 mm, which are relatively comparable to the control column, the use of GSS tubes increased stiffness by 29% compared to the control specimen C0. Furthermore, combining GSS tubes with ECC joints resulted in a stiffness increase of 134%.

4 Numerical Simulation

4.1 Model`s Construction

To analyze the behaviour of the tested columns under simulated conditions, three-dimensional nonlinear finite element models (FEM) have been developed using Abaqus simulation software. These models meticulously replicated the actual geometry of the columns, including the positioning and dimensions of the steel reinforcement bars and galvanized steel sheets, as detailed in Fig. 1 and Table 1.

The concrete column, incorporating NC, ECC, and HSFRC, was modeled using three-dimensional (3D) eight-node solid hexahedron-shaped brick elements (C3D8R) with a maximum size of 10 mm. This element size was carefully chosen based on a mesh sensitivity analysis to ensure the results are independent of the mesh itself. Similarly, the reinforcing steel, including both vertical bars and horizontal stirrups, was modeled with 3D two-node truss elements (T3D2) capable of carrying only axial forces. All steel bars were modeled as truss elements to reduce computational cost compared to modeling them as beam elements, especially; no dual action was noticed for all experimented columns as previously modelled (Hamoda et al., 2024b, 2024d, 2025). These steel elements utilized the same 10 mm size as the concrete elements. Finally, the GSS were modeled using the identical element type (C3D8R) and size (10 mm) as the concrete column, as illustrated in Fig. 7a, while the installed C0 model can be seen in Fig. 7b.

In the intermediate construction joint, the extended bars from each pre-cast column were spliced by aligning each bar beside its counterpart from the adjacent column, as illustrated in Fig. 7a. This configuration ensured proper load transfer and structural continuity. In the Abaqus simulation, the construction joint was defined as the host region, while the spliced bars were modeled as embedded elements within this host region. This modeling approach effectively captured the interaction between the embedded steel and the surrounding concrete, ensuring an accurate representation of the joint's behaviour under load.

The model simplifies the interaction between materials for computational efficiency. A perfect bonding was considered between the reinforcing bars and confined concrete, assuming the concrete as a single entity and the steel as embedded elements within it. Similarly, the contact between the concrete column and the surrounding GSS was modeled using a surface-to-surface approach. This approach incorporates two features: a penalty function with a friction coefficient of 0.6 in the tangential direction (allowing for some slippage), and hard contact in the normal direction (preventing separation). This same interaction method was applied between all concrete surfaces within the model but with a friction coefficient of 0.8. The results confirmed that the friction coefficients used herein (i.e., 0.6 and 0.8) are consistent with previously reported values (Hamoda et al., 2023b, 2023c, 2023d, 2024b, 2024c, 2024e, 2024f, 2025).

To accurately replicate the experimental setup, the finite element model mirrored the boundary conditions and loading scenario (Alharthai et al., 2024; Baktheer et al., 2024b; Hamoda et al., 2024a). The column's base was fixed in all directions, preventing any movement or rotation. Conversely, the top of the column was only free to move along the axial direction, which was where the load was applied. Coupling constraints were used to connect reference points on the top and bottom surfaces of the column to the applied restraints and load. To ensure a smooth transition at the beginning and end of the loading process, a gradually increasing amplitude was specified for the loading step, minimizing any sudden changes in kinetic energy.

4.2 Constitutive Modeling of Materials

This study considered both linear and nonlinear behavior for the concrete material in the model. Linear behavior relied on the Young's modulus and Poisson's ratio, presented in Table 3. To capture the more complex, nonlinear material behavior of concrete, the concrete damage plasticity (CDP) model was used. This model considers cracking under tension and crushing under compression as the two primary failure and dissipative mechanisms. For the nonlinear stress–strain relationship in compression, Eq. 3 developed by Wight and MacGregor (2005) as used:

$$\frac{f_c}{f_c'} = \frac{n\left(\frac{\varepsilon_c}{\varepsilon_0}\right)}{n-1+\left(\frac{\varepsilon_c}{\varepsilon_0}\right)^{nk}} \tag{3}$$

This equation incorporates the concrete compressive stress (f_c), the reference compressive strength based on a cylinder (f_c'), the strain at peak stress (ε_0) (Table 3), a curve-fitting factor (n), and a factor controlling the slope of the stress–strain response (k). Equations 4 and 5 define the specific values for n, and K:

$$n = 0.8 + \left(\frac{f_c'}{2500}\right) \tag{4}$$

$$k = \begin{cases} 1 & for\ \dfrac{\varepsilon_c}{\varepsilon_0} \le 1 \\ 0.67 + \left(\dfrac{f_c'}{9000}\right) & for\ \dfrac{\varepsilon_c}{\varepsilon_0} > 1 \end{cases} \tag{5}$$

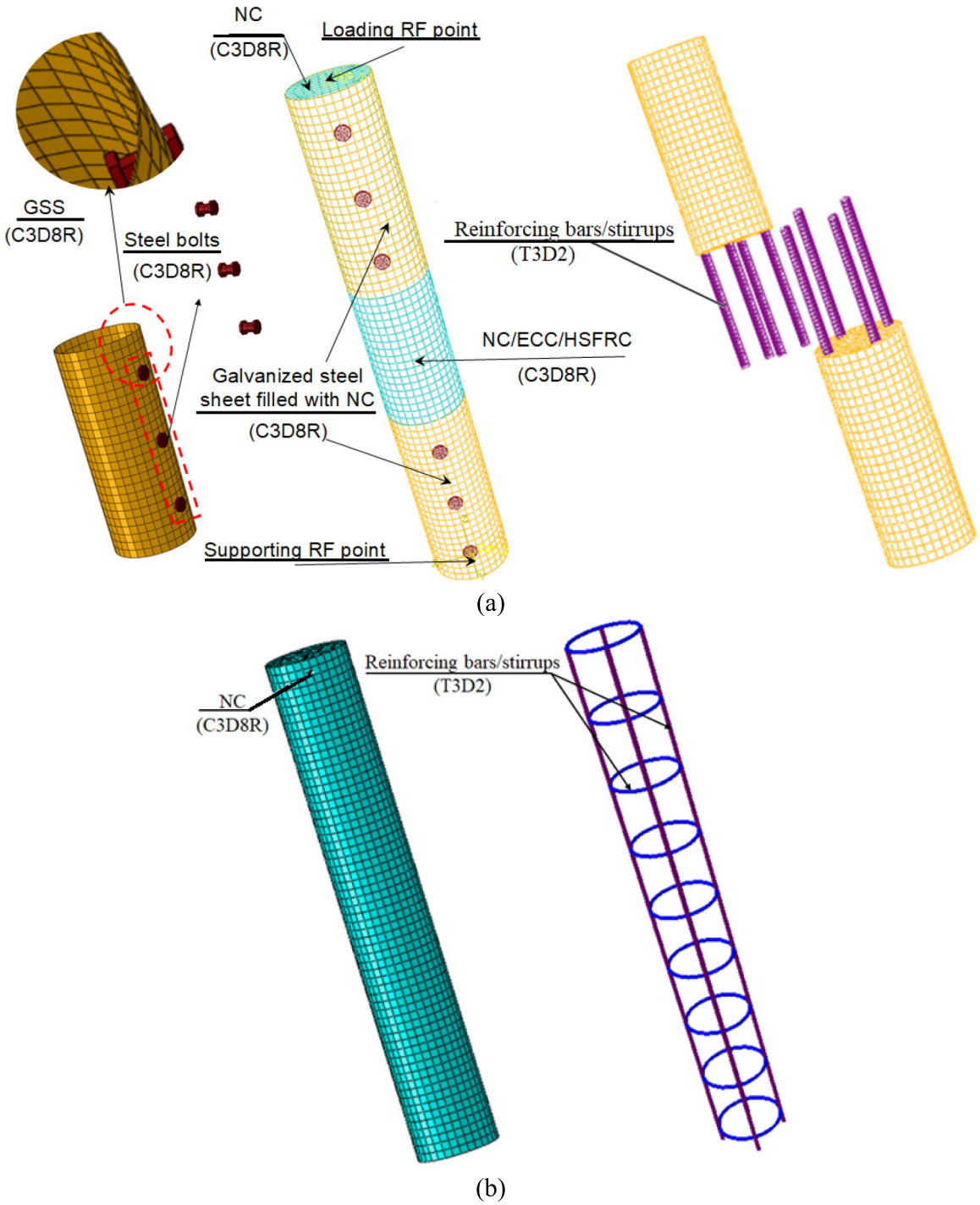

Fig. 7 Developed model. **a** CFST precast columns. **b** Column C0

This study adopted previously established stress–strain correlations for both ECC and HSFRC according to Zhou et al. (2015). These correlations, detailed in Eqs. 6 and 7 are grounded in comprehensive experimental results, providing a robust framework for understanding the stress–strain behavior of these advanced materials. Equation 5 characterizes the stress–strain curve under compression, while Eq. 5 represents the curve under tension as follows:

$$f_c = \begin{cases} E_0\varepsilon_c & \varepsilon_c \le 0.4\,\varepsilon_{cp} \\ E_0\varepsilon_c\left(1 - 0.308\,\dfrac{E_0\varepsilon_c}{f_c'} + 0.124\right) & 0.4\,\varepsilon_{cp} < \varepsilon_c \le \varepsilon_{cp} \end{cases} \tag{6}$$

$$f_t = \begin{cases} \dfrac{f_{tc}}{\varepsilon_{tc}}\varepsilon_t & 0 \le \varepsilon_t \le \varepsilon_{tc} \\ f_{tc} + \dfrac{f_{tu} - f_{tc}}{\varepsilon_{tu} - \varepsilon_{tc}}(\varepsilon - \varepsilon_{tc}) & \varepsilon_{tc} \le \varepsilon_t \le \varepsilon_{tu} \end{cases} \tag{7}$$

where the concrete's stiffness is denoted as (E_0) and strain at peak stress is (ε_{cp}). f_{t0} and ε_{tc} denote the concrete's tensile strength and strain at first crack. f_{tu} and ε_{tu} refer to tensile strength and its corresponding strain.

Table 5 CDP parameters

Concrete	ψ	ϵ	f_{b0}/f_{c0}	K	μ
NC	25	0.1	1.16	0.67	0.001
ECC	30				
HSFRC	30				

To simulate the behaviour of steel elements in a concrete column, a bi-linear elastic–plastic behaviour model with hardening was utilized. This model effectively represents two primary characteristics of steel: its initial elastic response under stress, followed by its transition to plastic deformation. The incorporation of hardening allows for a more accurate depiction of the steel's capacity to bear additional load after yielding, ensuring a realistic representation of the material's performance throughout the loading process. For defining the steel material properties, the actual methodology was employed based on the experimentally observed curved stress–strain response, which was then idealized linearly as shown in Fig. 2a to avoid the complicated model solving. This methodology is more reliable and has been executed in previous numerical studies (Hamoda et al., 2023b, 2023c, 2023d, 2024c, 2024e; Hu et al., 2024).

4.3 Sensitivity of Numerical CDP Parameters

This section focuses on two key aspects crucial for finite element modeling of concrete behavior: plasticity parameters and mesh size. The required plasticity parameters [Table 5; Emara et al., 2023; Hamoda et al., 2019, 2023a, 2023b, 2023c, 2023d, 2024b)] convert the uniaxial stress–strain relationship of concrete, which considers tension in one direction only, to a more realistic biaxial relationship that accounts for tension or compression in two directions. These parameters include the dilation angle (ψ), eccentricity (ϵ), biaxial-to-uniaxial yield stress ratio (f_{b0}/f_{c0}), ratio of tensile to compressive stress invariants (K), and the viscosity parameter (μ). In addition, the study investigated the impact of mesh size, a critical

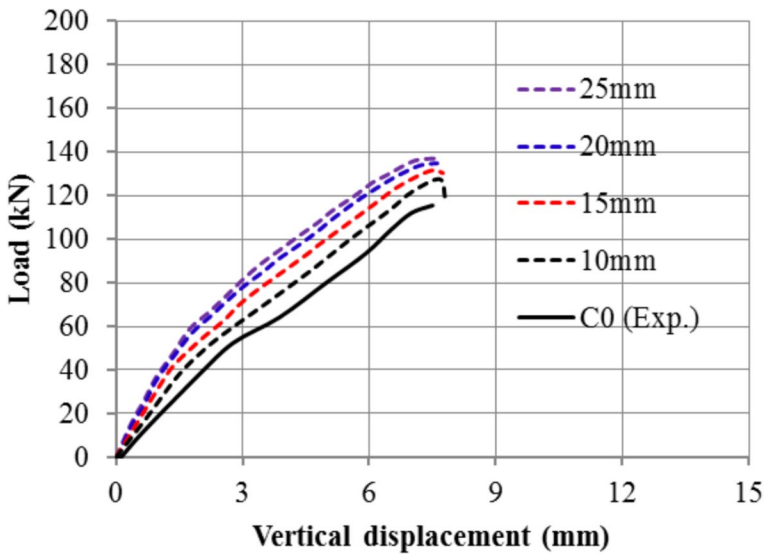

Fig. 8 Effect of mesh size

factor influencing accuracy and computational efficiency. A mesh size of 10 mm was found to provide acceptable results (see Fig. 8) without significantly increasing processing time. It is worth noting that the dilation angles differ according to the concrete types, as listed in Table 5, which can be attributed to variations in concrete composition, strength, and the level of confinement. The internal structure of the material and its degree of confinement determine the dilation angle, which is a measurement of how concrete expands under shear stress. These distinctions show how the mechanical characteristics of the various types of concrete cause them to react differently to applied stresses (Hamoda et al., 2019, 2023c, 2023d).

4.4 Initial Imperfection

In general, the reinforced concrete structural elements are exposed to effects of initially existing imperfections that can be attributed to geometric properties, construction process or boundary conditions (Chen et al., 2013; Hamoda et al., 2024e; Harvey & Cain, 2020; Liao et al., 2013). Several executions were attempted with various assumed eccentricities as a result of initial imperfection. Such imperfections were assumed to have the values varying from h/1000 up to h/400 at mid-height giving, where h is column length as previously reported (Hamoda et al., 2023a, 2024b). The imperfection value of L/400 presented satisfied exhibition for modelling both the ultimate capacity, mode of failure and load–displacement response development as shown in Figs. 8 and 9, respectively.

4.5 FEM Verification

To ensure the accuracy of the FEMs, their results were compared against those obtained from the experimental program. This validation process considered both the load versus axial displacement curve (Fig. 9) and the observed failure modes (Fig. 10). In addition, the numerical estimated absorbed energy can be seen in (Fig. 11) for sample E-L2. As can be seen in the figures,

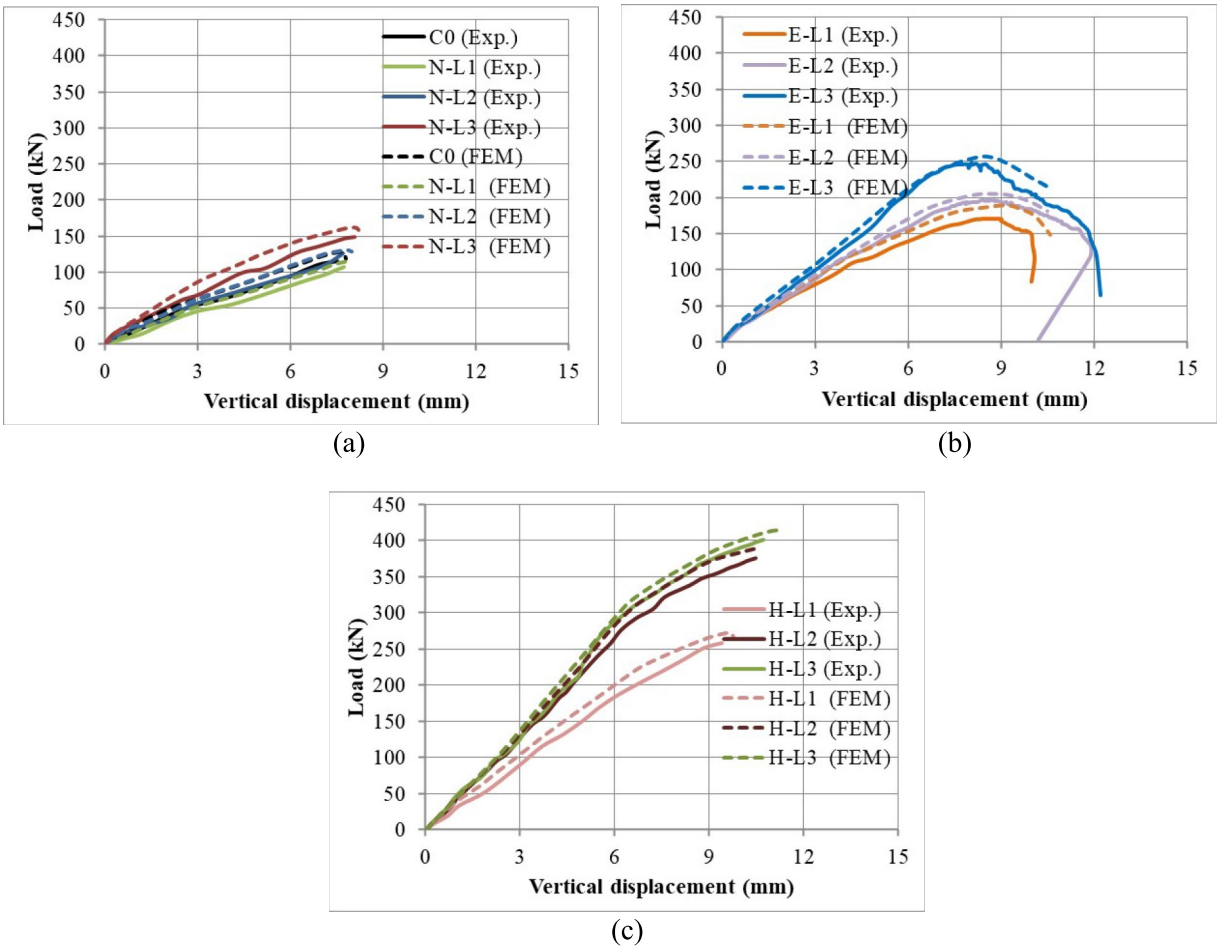

Fig. 9 FE versus experimental load–vertical displacement development: **a** Group GN, **b** Group GE, and **c** Group GH

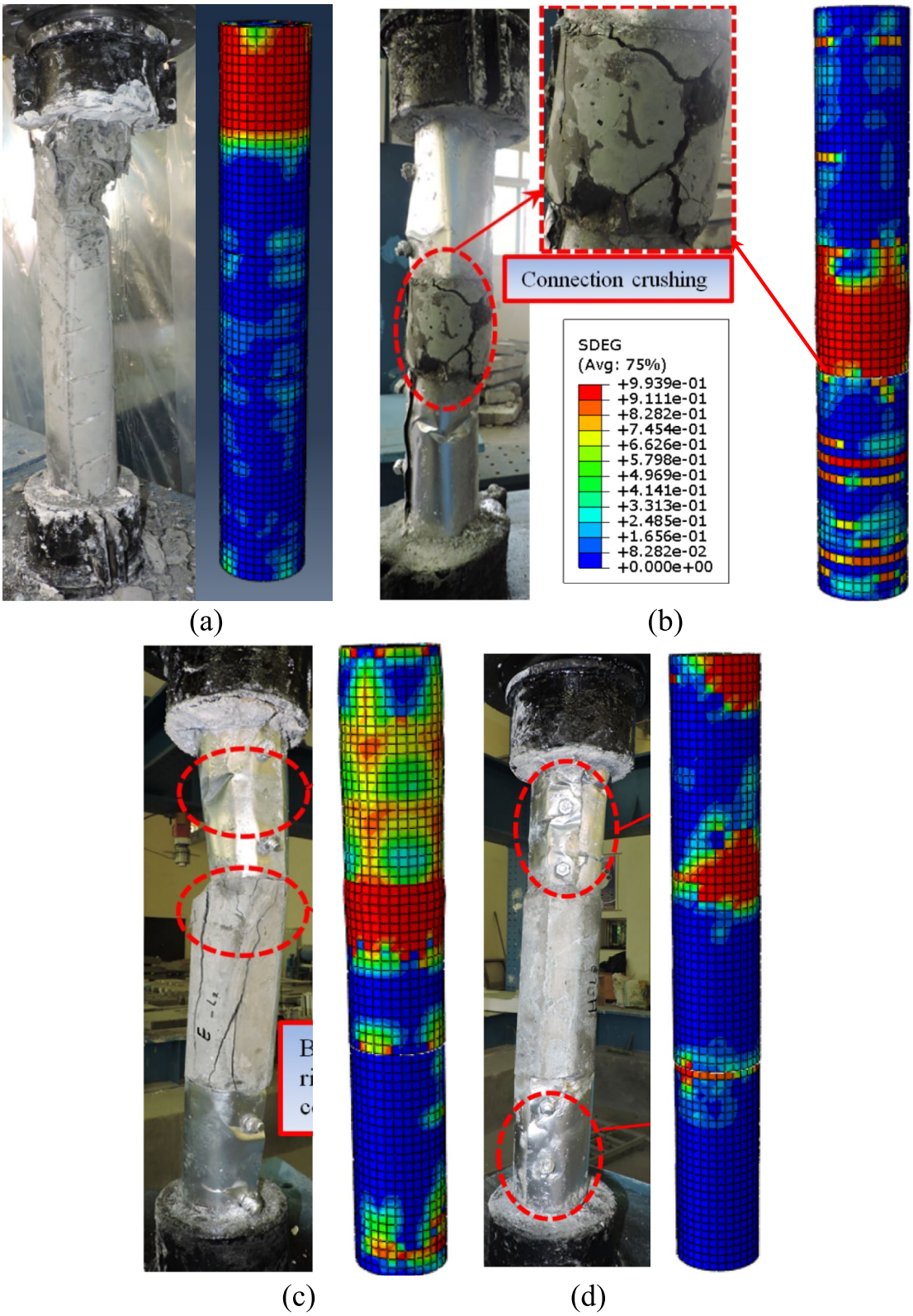

Fig. 10 FE versus experimental failure modes with respect to initial imperfection (Liao et al., 2013; Liu et al., 2023): **a** Column C0, **b** Column N-L1, **c** Column E-L2, and **d** Column H-L3

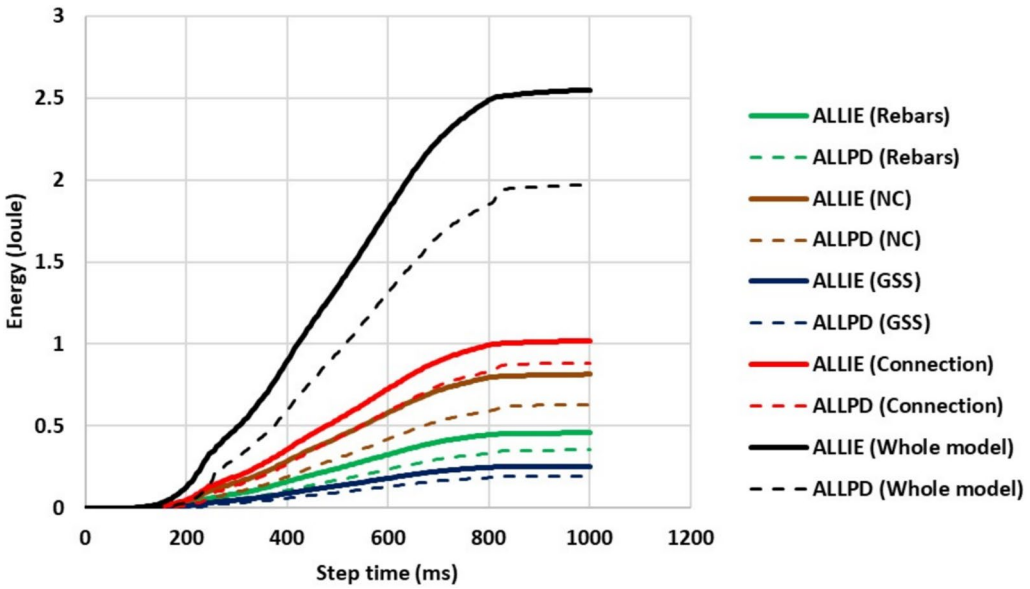

Fig. 11 Absorbed energy obtained numerically for Column E-L2

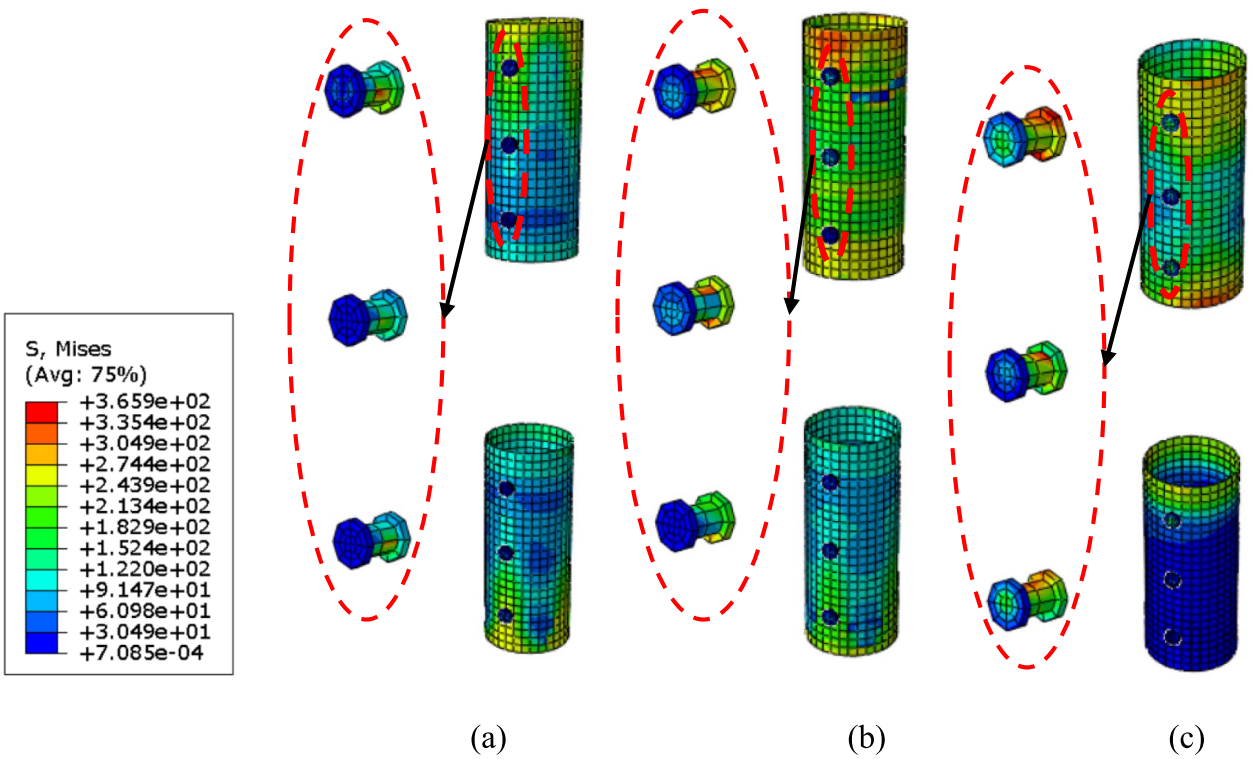

Fig. 12 Von misses stresses on GSS: **a** Column N-L1, **b** Column E-L2, and **c** Column H-L2

a good correlation was achieved between the FEM predictions and the experimental data for the tested columns. Notably, the FEMs slightly overestimate the maximum load-carrying capacity of the columns by approximately 10%, with a corresponding overestimation of displacement by around 2%. Moreover, the FEMs could reasonably simulate the cracking behaviors of tested columns and predict their failure modes, as

shown in Fig. 10. In addition, Fig. 12 shows the behavior of stresses formed on the CFST columns through von Mises stresses. Figure 12 confirms that the stresses occurred at both GSS tubs along with those on acting on blots were less than those generated at the connection. This may also confirm the avoidance of premature failures on bolts.

Plastic dissipation energy observed numerically (ALLPD) and internal potential energy (ALLPD) provided valuable insights into permanent deformations and structural damage, as it represents the energy consumed by irreversible processes within the material (Saad et al., 2023, 2024a). Notably, ALLPD is a subset of the total internal energy ALLIE (Dai et al., 2010; Saad et al., 2024b). Fig. 11 illustrates the evolution of plastic dissipation energy and internal potential energy during the loading process for the entire model and its key components: the normal concrete region, GSS parts, rebars, and the connection region. These components contribute 40%, 32%, 18%, and 10%, respectively, to the total internal energy (ALLIE), and 45%, 35%, 15%, and 0.1%, respectively, to the plastic dissipation energy (ALLPD). These findings from the energy analysis align well with the experimentally observed failure modes and deformations in the specimens.

4.6 Parametric Study

Having successfully validated the FEMs against experimental results, the researchers employed them for further parametric studies to explore the impact of two key factors on column capacity: GSS thickness and reinforcement ratio. The study investigated a range of GSS thicknesses (0.5, 0.7, 1.0, 1.2, and 1.5 mm) and reinforcement ratios (1.44%, 2.00%, 2.66%, and 4.00%). The observed relationships between load and vertical displacement are presented in Figs. 13 and 14.

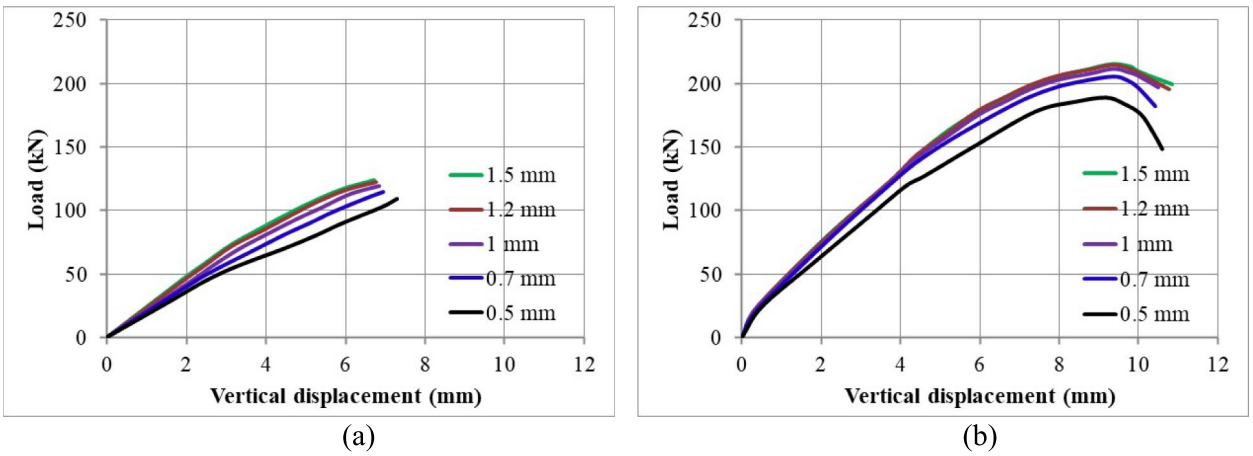

Fig. 13 Effect of GSS thickness: **a** NC and **b** ECC

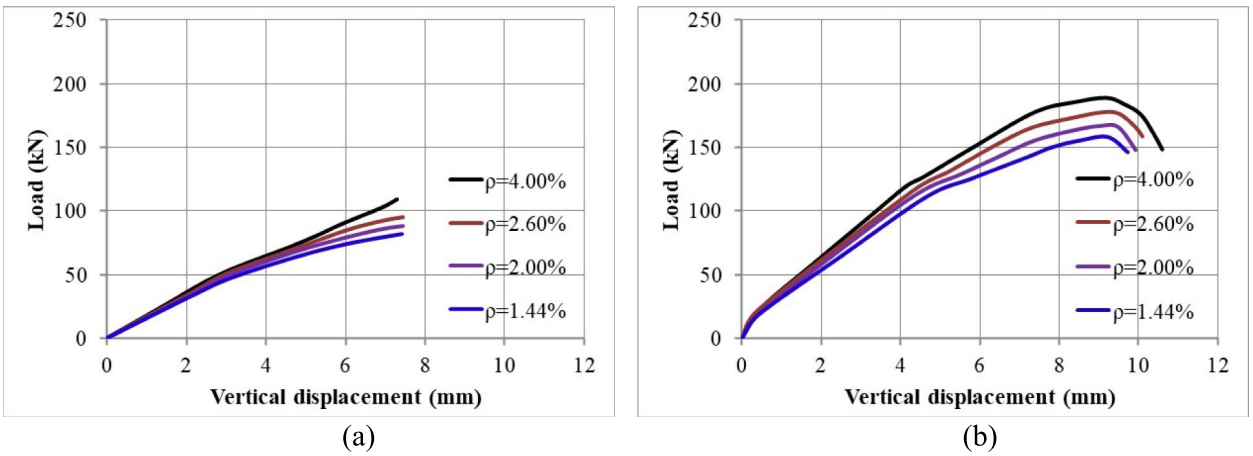

Fig. 14 Effect of reinforcement ratio: **a** NC and **b** ECC

Figure 13 clearly shows that increasing the thickness of the GSS leads to a minor, disproportionate increase in load-bearing capacity for both columns with NC and ECC joints (Fig. 13a). For the columns with NC joints, for example, increasing the GSS thickness from 0.5 mm up to 1.0 mm and 1.5 mm led to an increase in load-bearing capacity of 4% and 8%, respectively. Larger increases in load-bearing capacity were observed for columns with ECC joints (Fig. 13b). In particular, increasing the GSS thickness from 0.5 mm to 1.0 mm and 1.5 mm increased the ultimate load by 12% and 14%, respectively. These results illustrate the larger sensitivity of columns with ECC connection to the variations in GSS thickness compared to columns with NC joint.

The influence of the ratio of longitudinal reinforcement on the load–vertical displacement behavior for both column groups is shown in Fig. 14. A reduction in the reinforcement ratio for columns with NC joints from 4% to 2.6%, 2% and 1.44% led to a decrease in the ultimate bearing capacity by 17%, 24% and 29%, respectively. In the group of columns with ECC joints, a reduction of the reinforcement ratio from 4% to 2.6%, 2% and 1.44% led to a reduction of the ultimate load by 6%, 12% and 16%, respectively. These results emphasize the weaker influence of the longitudinal reinforcement ratio in columns with ECC joint compared to those with NC joint.

It is worth noting that the current study still has some imitations. First, only one test was performed for each parameter combination, which limits the possibility of performing a statistical analysis. Additional tests would be beneficial to confirm the reliability of the results. Second, while this research provides insight into the behavior of CFST columns with intermediate connections, future studies should compare these findings with pure CFST columns to better understand the impact of the connection on load-bearing capacity. Finally, while the Concrete Damage Plasticity model was used in this study, it has known limitations in capturing the full complexity of concrete behavior under various stress configurations, as noted in prior research [e.g., (Baktheer & Classen, 2024; Bažant et al., 2022)]. Future work may explore the use of more advanced macro- and meso-scale models to achieve more accurate predictions.

5 Conclusions

Based on the performed experimental study as well as numerical investigation of the CFST columns assembled with connecting joints, the following concluding remarks can be made:

1. The most common mode of failure of all CFST precast columns tested was a combined failure mode characterized by concrete crushing at the intermediate NC/ECC/HSFRC connection combined with rippling of the GSS of the tubular column.
2. The incorporation of GSS tubes with NC joint led to a notable 29% increase in the ultimate load in comparison with the control NC precast specimen. Furthermore, the combination of GSS tubes with ECC and HSFRC joints yielded significant enhancements in the ultimate load, with impressive increase by 115% and 247%, respectively.
3. The use of GSS tubes in the precast columns resulted in an improved energy absorption of 45% compared to the NC precast specimens. The incorporation of ECC and HSFRC connections together with the GSS tube resulted in a significant and remarkable improvement in the absorption of energy in the precast CFST column by 157% and 414%, respectively.
4. The integration of GSS tubes in the precast columns led to a 29% increase in elastic stiffness compared to the control specimen. Moreover, the combination of GSS tubes with ECC joints resulted in a significant stiffness enhancement of 134%.
5. The cracking force, ultimate force, elastic stiffness and energy absorption were found to show an increasing trend with the increase in the development length of the bars/splice joints for all joint types investigated.
6. The parametric studies conducted utilizing the validated 3D nonlinear finite element models revealed that variations in GSS thickness resulted in minimal effect on the columns load-bearing capacity of with intermediate connections. Conversely, alterations in the longitudinal reinforcement ratio exerted a more pronounced impact on the bearing amplitude of the columns.

Acknowledgements
The authors thank the support provided by Ongoing Research Funding Program, (ORF-2025–343), King Saud University, Riyadh, Saudi Arabia.

Author contributions
Ahmed Hamoda: conceptualization, methodology, software, validation, formal analysis, investigation, data curation, writing—original draft, visualization, and project administration. Aref A. Abadel: visualization, data curation, writing—review and editing, supervision, and funding aquistition. Abedulgader Baktheer: writing—original draft, validation, and funding aquistition. Mohamed Emara: writing—review and editing, data curation, and visualization.

Funding
Open Access funding enabled and organized by Projekt DEAL. The work is funded by King Saud University in Riyadh, Saudi Arabia, and by the personal funds of the first author.

Availability of data and materials
The data that support the findings of this study are available from the corresponding author upon reasonable request.

Declarations

Ethics approval and consent to participate
Not applicable.

Consent for publication
Not applicable.

Competing interests
The authors declare that they have no competing interests.

Received: 11 July 2024 Accepted: 14 March 2025
Published: 4 September 2025

References

Abadel, A. A., Baktheer, A., Emara, M., Ghallah, M., & Hamoda, A. (2024). Flexural behavior of precast concrete-filled steel tubes (CFST) connected with high-performance concrete joints. *Materials Science Poland*. https://doi.org/10.2478/msp-2024-0032

Abadel, A. A., Masmoudi, R., & Iqbal Khan, M. (2022). Axial behavior of square and circular concrete columns confined with CFRP sheets under elevated temperatures: Comparison with welded-wire mesh steel confinement. *Structures, 45*, 126–144. https://doi.org/10.1016/j.istruc.2022.09.026

ACI 318-19, Building Code Requirements for Structural Concrete and Commentary, Farmington Hills, Michigan, USA, Michigan, USA, 2019.

Alharthai, M., Bahrami, A., Badawi, M., Ghalla, M., Elsamak, G., & Abdelmgeed, F. A. (2024). Numerical study on enhancing shear performance of RC beams with external aluminum alloy plates bonded using steel anchors. *Results Eng., 22*, 102143. https://doi.org/10.1016/j.rineng.2024.102143

Baktheer, A., & Classen, M. (2024). A review of recent trends and challenges in numerical modeling of the anisotropic behavior of hardened 3D printed concrete. *Additive Manufacturing, 89*, 104309. https://doi.org/10.1016/j.addma.2024.104309

Baktheer, A., Goralski, C., Hegger, J., & Chudoba, R. (2024a). Stress configuration-based classification of current research on fatigue of reinforced and prestressed concrete. *Structural Concrete, 25*, 1765–1781. https://doi.org/10.1002/suco.202300667

Baktheer, A., Martínez-Pañeda, E., & Aldakheel, F. (2024b). Phase field cohesive zone modeling for fatigue crack propagation in quasi-brittle materials. *Computer Methods in Applied Mechanics and Engineering, 422*, 116834. https://doi.org/10.1016/j.cma.2024.116834

Baktheer, A., Spartali, H., Chudoba, R., & Hegger, J. (2022). Concrete splitting and tip-bearing effect in the bond of anchored bars tested under fatigue loading in the push-in mode: An experimental investigation. *Materials and Structures, 55*, 101. https://doi.org/10.1617/s11527-022-01935-7

Bažant, Z., Nguyen, H. T., & Abdullah Dönmez, A. (2022). Critical comparison of phase-field, peridynamics, and crack band model M7 in light of gap test and classical fracture tests. *Journal of Applied Mechanics*. https://doi.org/10.1115/1.4054221

Chen, J. F., Li, S. Q., & Bisby, L. A. (2013). Factors affecting the ultimate condition of FRP-wrapped concrete columns. *Journal of Composites for Construction, 17*, 67–78. https://doi.org/10.1061/(ASCE)CC.1943-5614.0000314

Chiadighikaobi, P. C., Hasanzadeh, A., Hematibahar, M., Kharun, M., Mousavi, M. S., Stashevskaya, N. A., & Adegoke, M. A. (2024). Evaluation of the mechanical behavior of high-performance concrete (HPC) reinforced with 3D-Printed trusses. *Results Engineering, 22*, 102058. https://doi.org/10.1016/j.rineng.2024.102058

Ci, J., Ahmed, M., Liang, Q., Chen, S., Chen, W., Sennah, K., Hamoda, A. Behavior and design of circular concrete-filled double steel tubular slender columns under axial Loading, in: 7th Int. Conf. Civil, Struct. Transp. Eng., Avestia Publishing, Niagara Falls, Canada., 2022. https://doi.org/10.11159/iccste22.218.

Ci, J., Ahmed, M., Liang, Q. Q., Chen, S., Chen, W., Sennah, K., & Hamoda, A. (2022a). Experimental and numerical investigations into the behavior of circular concrete-filled double steel tubular slender columns. *Engineering Structures, 267*, 114644. https://doi.org/10.1016/j.engstruct.2022.114644

Dai, X. H., Wang, Y. C., & Bailey, C. G. (2010). Numerical modelling of structural fire behaviour of restrained steel beam–column assemblies using typical joint types. *Engineering Structures, 32*, 2337–2351. https://doi.org/10.1016/j.engstruct.2010.04.009

Dong, B., Pan, J., & Xu, L. (2022). Numerical and theoretical analysis of beam-to-column connections with ECC ring beams subjected to local compression loading. *Journal of Building Engineering, 52*, 104466. https://doi.org/10.1016/j.jobe.2022.104466

ECP (203-2018), Permanent Committee for the Code of Practice for Reinforced Concrete Structures, Ministry of Housing, Utilities and Urban Development, Arab Republic of Egypt, 2018.

Ekmekyapar, T., & AEliwi, B. J. M. (2016). Experimental behaviour of circular concrete filled steel tube columns and design specifications. *Thin-Walled Structure, 105*, 220–230. https://doi.org/10.1016/j.tws.2016.04.004

Elwood, K. J., & Eberhard, M. O. (2009). Effective stiffness of reinforced concrete columns. *ACI Structural Journal*. https://doi.org/10.14359/56613

Emara, M., Hamoda, A., & Hu, J. W. (2023). Numerical assessment of rectangular one-and two-way RC slabs strengthened with CFRP under impact loads. *Computers and Concrete, 31*, 173. https://doi.org/10.12989/cac.2023.31.3.173

Fang, Y., Wang, Y., Hou, C., & Lu, B. (2020). CFDST stub columns with galvanized corrugated steel tubes: Concept and axial behaviour. *Thin-Walled Structure, 157*, 107116. https://doi.org/10.1016/j.tws.2020.107116

Fayed, S., Madenci, E., Onuralp Özkiliç, Y., & Mansour, W. (2023). Improving bond performance of ribbed steel bars embedded in recycled aggregate concrete using steel mesh fabric confinement. *Construction and Building Materials, 369*, 130452. https://doi.org/10.1016/j.conbuildmat.2023.130452

Gopal, S. R., & Manoharan, P. D. (2006). Experimental behaviour of eccentrically loaded slender circular hollow steel columns in-filled with fibre reinforced concrete. *Journal of Constructional Steel Research, 62*, 513–520. https://doi.org/10.1016/j.jcsr.2005.09.004

Gu, C., Wang, X., Zhou, X., Li, X., Liao, Y., & Zheng, N. (2024). Seismic behavior of prefabricated thin-walled CFST double-column bridge piers. *Thin-Walled Struct., 198*, 111654. https://doi.org/10.1016/j.tws.2024.111654

Hamoda, A., Abadel, A. A., Shahin, R. I., Ahmed, M., Baktheer, A., & Yehia, S. A. (2024). Shear strengthening of simply supported deep beams using galvanized corrugated sheet filled with high-performance concrete. *Case Studies in Construction Materials, 21*, e04085. https://doi.org/10.1016/j.cscm.2024.e04085

Hamoda, A. A., Ahmed, M., Abadel, A. A., Ghalla, M., Patel, V. I., & Liang, Q. Q. (2023a). Experimental and numerical studies of circular precast concrete slender columns with intermediate connection filled with high-performance concrete. *Structures, 57*, 105204. https://doi.org/10.1016/j.istruc.2023.105204

Hamoda, A., Ahmed, M., Abadel, A. A., & Gohari, S. (2024b). Experimental and numerical investigations of precast circular reinforced concrete slender columns with intermediate connection. *Advances in Structural Engineering, 27*, 373–385. https://doi.org/10.1177/13694332231222091

Hamoda, A., Ahmed, M., Ghalla, M., Liang, Q. Q., & Abadel, A. A. (2023b). Flexural performance of precast circular reinforced concrete members with intermediate connection filled with ultra-high-performance-concrete. *Case Studies in Construction Materials, 19*, e02386. https://doi.org/10.1016/j.cscm.2023.e02386

Hamoda, A., El-Mandouh, M. A., Ahmed, M., Abadel, A. A., Liang, Q. Q., & Elsamak, G. (2023d). Experimental and numerical studies of reinforced concrete stair beams strengthened with steel bars and plates. *Engineering Structures, 297*, 117037. https://doi.org/10.1016/j.engstruct.2023.117037

Hamoda, A., Emara, M., Abdelazeem, F., & Ahmed, M. (2023c). Experimental and numerical analysis of RC beams strengthened with ECC and stainless steel strips. *Magazine of Concrete Research, 75*, 251–270. https://doi.org/10.1680/jmacr.22.00127

Hamoda, A., Emara, M., & Mansour, W. (2019). Behavior of steel I-beam embedded in normal and steel fiber reinforced concrete incorporating

demountable bolted connectors. *Composites. Part b, Engineering, 174*, 106996. https://doi.org/10.1016/j.compositesb.2019.106996
Hamoda, A., Ghalla, M., Yehia, S. A., Ahmed, M., Abadel, A. A., Baktheer, A., & Shahin, R. I. (2024). Experimental and numerical investigations of the shear performance of reinforced concrete deep beams strengthened with hybrid SHCC-mesh. *Case Studies in Construction Materials*. https://doi.org/10.1016/j.cscm.2024.e03495
Hamoda, A., Sennah, K., Abadel, A. A., & Emara, M. (2024). Strengthening of interior circular column-slab region incorporating combinations of bonded UHPECC layer, CFRP sheets, and threaded steel bolts. *Structures, 69*, 107545. https://doi.org/10.1016/j.istruc.2024.107545
Hamoda, A., Shahin, R. I., Abadel, A. A., Sennah, K., Ahmed, M., & Yehia, S. A. (2025). Shear strengthening of normal concrete deep beams with openings using strain-hardening cementitious composites with glass fiber mesh. *Structures, 71*, 107994. https://doi.org/10.1016/j.istruc.2024.107994
Hamoda, A., Shahin, R. I., Ahmed, M., Abadel, A. A., Baktheer, A., & Yehia, S. A. (2024a). Strengthening of reinforced concrete columns incorporating different configurations of stainless-steel plates. *Structures, 64*, 106577. https://doi.org/10.1016/j.istruc.2024.106577
Hamoda, A., Yehia, S. A., Ahmed, M., Abadel, A. A., Baktheer, A., & Shahin, R. I. (2024). Experimental and numerical analysis of deep beams with openings strengthened with galvanized corrugated and flat steel sheets. *Case Studies in Construction Materials*. https://doi.org/10.1016/j.cscm.2024.e03522
Harvey, P. S., & Cain, T. M. N. (2020). Buckling of elastic columns with initial imperfections and load eccentricity. *Structures, 23*, 660–664. https://doi.org/10.1016/j.istruc.2019.09.021
Hossain, K. M. A., Hamoda, A. A., Sennah, K., Shoukry, M. E., & Mahmoud, Z. I. (2015). Bond strength of ribbed GFRP bars embedded in high performance fiber reinforced concrete. *Journal of Multidisciplinary Engineering Science and Technology, 2*, 1260.
Hu, H.-S., Yang, Z.-J., Xu, L., Zhang, Y.-X., & Gao, Y.-C. (2023). Axial compressive behavior of square concrete-filled steel tube columns with high-strength steel fiber-reinforced concrete. *Engineering Structures, 285*, 116047. https://doi.org/10.1016/j.engstruct.2023.116047
Hu, J.-Y., Hong, W.-K., & Park, S.-C. (2017). Experimental investigation of precast concrete based dry mechanical column–column joints for precast concrete frames. *The Structural Design of Tall and Special Buildings, 26*, e1337. https://doi.org/10.1002/tal.1337
Hu, J., Wei, Y., Yi, J., Zhang, Y., & Zhao, K. (2024). Axial compression performance of underwater columns reinforced with stainless steel tube-FRP grids. *Journal of Constructional Steel Research, 218*, 108721. https://doi.org/10.1016/j.jcsr.2024.108721
Huang, Z., Zheng, K., Wei, Y., Wang, G., & Zhang, Y. (2023). Axial compressive behaviour of SWSSC-filled stainless steel tube columns with in-built CFRP or stainless steel tubes. *Journal of Building Engineering, 72*, 106543. https://doi.org/10.1016/j.jobe.2023.106543
Hung, C.-C., Hsiao, H.-J., Shao, Y., & Yen, C.-H. (2023). A comparative study on the seismic performance of RC beam-column joints retrofitted by ECC, FRP, and concrete jacketing methods. *J. Build. Eng., 64*, 105691. https://doi.org/10.1016/j.jobe.2022.105691
Isleem, H. F., Chukka, N. D. K. R., Bahrami, A., Oyebisi, S., Kumar, R., & Qiong, T. (2023). Nonlinear finite element and analytical modelling of reinforced concrete filled steel tube columns under axial compression loading. *Results in Engineering, 19*, 101341. https://doi.org/10.1016/j.rineng.2023.101341
Kuttab, A., & Dougill, J. W. (1988). Grouted and dowelled jointed precast concrete columns: Behaviour in combined bending and compression. *Magazine of Concrete Research, 40*, 131–142. https://doi.org/10.1680/macr.1988.40.144.131
Lai, B.-L., Zhang, M.-Y., Zheng, X.-F., Chen, Z.-P., & Zheng, Y.-Y. (2023). Experimental study on the axial compressive behaviour of steel reinforced concrete composite columns with stay-in-place ECC jacket. *Journal of Building Engineering, 68*, 106174. https://doi.org/10.1016/j.jobe.2023.106174
Li, P., Chen, Y., & Yuan, F. (2023). Stress-strain behavior of ECC-GFRP spiral confined concrete cylinders. *Journal of Building Engineering, 63*, 105473. https://doi.org/10.1016/j.jobe.2022.105473
Liao, F.-Y., Han, L.-H., & Tao, Z. (2013). Behaviour of CFST stub columns with initial concrete imperfection: Analysis and calculations. *Thin-Walled Structure, 70*, 57–69. https://doi.org/10.1016/j.tws.2013.04.012
Liu, J., Gao, P., Lin, X., Wang, X., Zhou, X., & Chen, Y. F. (2023). Experimental assessment on the size effects of circular concrete-filled steel tubular columns under axial compression. *Engineering Structures, 275*, 115247. https://doi.org/10.1016/j.engstruct.2022.115247
Ma, Y., Che, Y., & Gong, J. (2012). Behavior of corrosion damaged circular reinforced concrete columns under cyclic loading. *Construction and Building Materials, 29*, 548–556. https://doi.org/10.1016/j.conbuildmat.2011.11.002
MacGregor, J. G., Wight, J. K., Teng, S., Irawan, P. (2005). Reinforced concrete: Mechanics and design
Obaidat, A. T., Ashteyat, A. M., Hanandeh, S., & Al-Btoush, A. Y. (2020). Behavior of heat damaged circular reinforced concrete columns repaired using Carbon Fiber Reinforced Polymer rope. *Journal of Building Engineering, 31*, 101424. https://doi.org/10.1016/j.jobe.2020.101424
Punurai, W., Hsu, C.-T.T., Punurai, S., & Chen, J. (2013). Biaxially loaded RC slender columns strengthened by CFRP composite fabrics. *Engineering Structures, 46*, 311–321. https://doi.org/10.1016/j.engstruct.2012.07.014
Rave-Arango, J. F., Blandón, C. A., Restrepo, J. I., & Carmona, F. (2018). Seismic performance of precast concrete column-to-column lap-splice connections. *Engineering Structures, 172*, 687–699. https://doi.org/10.1016/j.engstruct.2018.06.049
Saad, A. G., Sakr, M. A., Khalifa, T. M., & Darwish, E. A. (2023). Numerical analysis of rubberized engineered cementitious composite (RECC) RC beams under impact loads. *Construction and Building Materials, 409*, 134162. https://doi.org/10.1016/j.conbuildmat.2023.134162
Saad, A. G., Sakr, M. A., Khalifa, T. M., & Darwish, E. A. (2024a). Shear behavior of RC beams with openings under impact loads: Unveiling the effects of HSC and RECC. *Arch. Civ. Mech. Eng., 24*, 236. https://doi.org/10.1007/s43452-024-01041-1
Saad, A. G., Sakr, M. A., Khalifa, T. M., & Darwish, E. A. (2024b). Structural performance of concrete reinforced with crumb rubber: A review of current research. *Iranian Journal of Science and Technology, Transactions of Civil Engineering*. https://doi.org/10.1007/s40996-024-01629-w
Saatcioglu, M., & Ozcebe, G. (1989). Response of reinforced concrete columns to simulated seismic loading. *ACI Structural Journal*. https://doi.org/10.14359/2607
Tadi Beni, M. B., & Madhkhan, M. (2022). Experimental study on two innovative ductile moment-resisting precast concrete beam-column connections. *Structures, 39*, 559–572. https://doi.org/10.1016/j.istruc.2022.03.059
Tullini, N., & Minghini, F. (2016). Grouted sleeve connections used in precast reinforced concrete construction – Experimental investigation of a column-to-column joint. *Engineering Structures, 127*, 784–803. https://doi.org/10.1016/j.engstruct.2016.09.021
Wang, G., Li, Y., Li, Z., & Ingham, J. M. (2020). Experimental and numerical study of precast concrete columns with hybrid bolted splice connections. *Structures, 28*, 17–36. https://doi.org/10.1016/j.istruc.2020.08.042
Wei, J., Liu, H., & Leung, C. K. Y. (2022). Application of high-strength strain-hardening cementitious composites (SHCC) in the design of novel inter-module joint. *Construction and Building Materials, 359*, 129491. https://doi.org/10.1016/j.conbuildmat.2022.129491
Xiong, M.-X., Ren, T., Zhou, P., Yang, M., Gong, W., & Li, H. (2024). Post-fire compressive behavior of CFRP stirrups reinforced CFST columns: Experimental investigation and calculation models. *Thin-Walled Structure, 198*, 111747. https://doi.org/10.1016/j.tws.2024.111747
Xu, C., Chen, D., Miramini, S., Liu, X., Xu, W., & Zhang, L. (2023). Experimental fire performance assessment of a new type of prestressed composite circular precast concrete columns. *Engineering Structures, 278*, 115509. https://doi.org/10.1016/j.engstruct.2022.115509
Xu, Y., Jia, Y., Tong, Z., & Shivahari, S. (2021). Cyclic loading test for concrete bridge columns integrated with ECC segment at the plastic zone. *Engineering Structures, 246*, 112985. https://doi.org/10.1016/j.engstruct.2021.112985
Zhang, Z., Wu, X., Sun, Q., Tian, P., & Hu, G. (2023). Compressive behavior of corroded reinforced concrete columns strengthened with BFRP reinforced ECC in marine environment. *Ocean Engineering, 279*, 114533. https://doi.org/10.1016/j.oceaneng.2023.114533
Zhou, J., Pan, J., & Leung, C. K. Y. (2015). Mechanical behavior of fiber-reinforced engineered cementitious composites in uniaxial compression. *Journal of Materials in Civil Engineering, 27*, 04014111. https://doi.org/10.1061/(ASCE)MT.1943-5533.0001034

Zhou, X., Wang, X., Gu, C., Chung, K.-F., Liu, J., Liao, Y., & Chen, X. (2023). Seismic behavior of a novel prefabricated thin-walled CFST double-column pier system for simple on-site assembly. *Thin-Walled Structure, 183*, 110388. https://doi.org/10.1016/j.tws.2022.110388

Publisher's Note

Ahmed Hamoda Assistant Professor at the Civil Engineering Department, Faculty of Engineering, Kafrelsheikh University, Kafrelsheikh, Egypt.

Aref A. Abadel Associate Professor at the Department of Civil Engineering, College of Engineering, King Saud University, Riyadh 11421, Saudi Arabia

Abedulgader Baktheer Postdoctoral Researcher at the Institute of Mechanics and Computational Mechanics, Leibniz Universität Hannover, Hannover, Germany.

Mohamed Emara Associate Professor at the Structural Engineering Department, Faculty of Engineering, Zagazig University, Zagazig, Egypt.